

Investigating the accelerated expansion of the Universe through updated constraints on viable $f(R)$ models within the metric formalism

Kumar Ravi^{1,*}, Anirban Chatterjee^{2,†}, Biswajit Jana^{1,‡} and Abhijit Bandyopadhyay^{1,§}

¹*Department of Physics, Ramakrishna Mission Vivekananda Educational and Research Institute, Belur Math 711202, West Bengal, India*

²*Department of Physics, Indian Institute of Technology Kanpur, Kanpur 208016, UP, India*

(Dated: June 23, 2023)

Modified theories of gravity encompass a class of $f(R)$ -models that seek to elucidate the observed late time accelerated expansion of the universe. In this study, we examine a set of viable $f(R)$ models (Hu-Sawicki: two cases, Satrobinsky, Tsujikawa, exponential and arcTanh models) in metric formalism, using recent cosmological data sets: type Ia supernovae data, cosmic chronometer observations, baryonic acoustic oscillations data, data from HII starburst galaxies, and local measurements of the Hubble parameter (H_0). We re-parameterize the $f(R)$ models using a distortion/deviation parameter (b) which is a measure of their deviation from the standard Λ CDM model. The model parameters are constrained using a Bayesian analysis with the Monte Carlo Markov Chain method. We employ statistical tools such as the Akaike Information Criterion, Bayesian Information Criterion, and reduced chi-square statistics to conduct a comparative investigation of these models. We determine the transition redshift, the evolution of total equation-of-state (EoS) parameter, and the EoS for the component responsible for current accelerated expansion to characterize the expansion's evolution. Taking into account the ‘‘Hubble tension,’’ we perform the study with and without a Gaussian prior for H_0 from local measurements. Our findings are as follows: (i) in many cases the $f(R)$ models are strongly favored over the standard Λ CDM model, (ii) the deviation parameter (b) significantly deviates from zero in several cases, (iii) the inclusion of local H_0 not only increases the fitted value of H_0 (as expected) but also affects the gap between predictions of $f(R)$ models and the Λ CDM model, and (iv) the relevant quantities characterizing the (accelerated) expansion of the universe obtained in our models are consistent with those obtained in a model-independent way by others. Our investigation and results present a compelling case for pursuing further research on $f(R)$ models with future observations to come.

I. INTRODUCTION

In the last two decades, cosmological investigations have revealed an accelerated expansion of the current universe and have also identified a transition from a decelerating phase to the current accelerated phase occurring during the late time phase of cosmic evolution. The first empirical aspect of discovering this phenomenon came from the interpretation of luminosity distance and redshift measurements of type Ia supernovae (SNe Ia) events [1–4]. Furthermore, observation of baryon acoustic oscillations [5, 6], analysis of cosmic microwave background radiation [7–10], and examination of the power spectrum of matter distributions in the universe [11, 12] have substantiated evidence of this late-time cosmic acceleration. A general label describing the origin of the observed late time cosmic acceleration is ‘‘Dark energy’’ which refers to a theoretical unclustered form of energy exerting a negative pressure to counteract the gravitational attraction and thereby causing the cosmic acceleration.

Despite extensive research over many years, the true nature and origin of dark energy remains an enigma. Various theoretical perspectives have emerged, each attempting to construct models that can explain the observed cosmic acceleration. The introduction of the Λ term into Einstein's equation, known as the ‘‘A Cold Dark Matter (Λ CDM) model’’, is the simplest model that can explain the present accelerated expansion of the universe. However, this model encounters several challenges, such as the cosmic coincidence issue [13] and the fine-tuning problem [14] when considered in the context of particle physics. This motivates development and exploration of alternative dark energy models from a range of perspectives. An important class comprises field theoretic models that involve the incorporation of a scalar field within the energy-momentum tensor of the Einstein equation. The scalar field plays the role in generating the necessary negative pressure to drive cosmic acceleration, either through the slowly varying potentials (quintessence models [15]) or by means of their kinetic energy (k-essence models [16]).

Within the context of this study, another crucial category of models under consideration is modified gravity models which attempt to explain the acceleration through the geometry itself without modifying the energy-momentum tensor of the Einstein equation. These models primarily involve modifications to the geometric component of Einstein's equation, which may result from higher-order corrections to the Einstein-

* Corresponding Author: simplyravi@gmail.com

† anirbanc@iitk.ac.in

‡ vijnanachaitanya2020@gmail.com

§ abhijit@rkmvu.ac.in

Hilbert action. By introducing suitable modifications, it becomes feasible to induce cosmic acceleration. The most straightforward types of modifications involve the extension of the Ricci scalar R to an arbitrary function $f(R)$. The meticulous choice with appropriate justification of this particular arbitrary function play a crucial role in all modified gravity models. Theoretical considerations, like the need for a ghost-free theory with stable perturbations and the presence of Noether symmetries, impose initial constraints on the forms of the arbitrary function $f(R)$. However, ability to reproduce the observed features of cosmic evolution, the behavior of local (solar) systems etc. also serve as the primary tool to further constrain the $f(R)$ -models.

In this study, our objective is to provide updated constraints on viable $f(R)$ gravity models using the latest cosmological data, including supernovae type Ia(SNIa) from Pantheonplus compilation, cosmic chronometer(CC) observations, baryonic acoustic oscillations(BAO) data, HII starburst galaxies(HIIG) data, and data from local measurements of the Hubble parameter (H_0). Specifically, we focus on six viable $f(R)$ models: the Hu-Sawicki model(two cases), the Starobinsky model, the exponential model, the Tsujikawa model, and the arc-Tanh model. By considering these models, we obtained an update of best-fit values and uncertainties at different confidence levels of the associated parameters of the models. We have chosen these particular $f(R)$ gravity models because most of the modified gravity models either fail to explain the matter-dominated era or have already been ruled out by observational data sets. The selected models, mentioned above, represent a few remaining options to study the impact of modified gravity theory within the framework of metric or Palatini formalism. For our investigation, we adopt the metric formalism techniques in the context of a homogeneous and isotropic universe. Rather than working with original forms of these $f(R)$ models(which for some models give a false impression that they are non-reducible to the Λ CDM model), we chose to re-parameterize these models in terms of what is called “deviation/distortion parameter(b)”. In this form, with $b \rightarrow 0$, a $f(R)$ model tends to the Λ CDM model.

The current state of research in this specific context, which involves constraining various $f(R)$ models within the metric formalism using cosmologically relevant data, is experiencing a high level of activity. Here we refer to several such relevant previous works. In [17], the authors obtained constraints on the Hu-Sawicki and the Starobinsky models by utilizing approximate analytical solutions derived from Taylor series expansions for the Hubble parameter. The constraints were derived using SNIa data from Union 2.1 compilation, BAO data, cosmic microwave background (CMB) shift parameter data and growth rate data. In [18], the constraints on Hu-Sawicki, Starobinsky, exponential, and Tsujikawa models were obtained by utilizing CC data, local measurements of H_0 , SNIa data from the

Joint-Lightcurve-Analysis (JLA) compilation, and BAO data. Furthermore, [19] constrained the exponential model using SNIa (Union 2.1), CC, BAO, and CMB data, while also discussing the viability of this model in describing the entire cosmological history. Exploration of various $f(R)$ models, including the Hu-Sawicki and the exponential models, with data sets such as SNIa (JLA), CC, BAO, CMB, local H_0 , and growth rate, was conducted in [20]. Other significant works that investigated Hu-Sawicki and/or exponential models, utilizing various data sets including gravitational lensing data, are [21–23]. In [24], constraints on Hu-Sawicki, Starobinsky, exponential, and Tsujikawa models were examined in both flat and non-flat spacetimes, utilizing various cosmological data sets. Recently, [25] have advocated for the use of quasar X-ray and UV fluxes data to investigate $f(R)$ models and have constrained Hu-Sawicki and exponential models accordingly. Moreover, the Taylor series approach from [17] was extended to include the arcTanh model in [26]. Using Gaussian process reconstruction of the Hubble diagram with CC and HIIG data, the parameters of these three $f(R)$ models were determined.

This paper is organised as follows. In Section II we derive the modified Friedmann equations and other relevant equations from the action for $f(R)$ gravity. Section III covers discussions of the conditions that any viable $f(R)$ models must satisfy, along with brief introductions of the specific $f(R)$ models investigated in this work. In Section IV, we introduce the cosmological data sets and the corresponding equations that establish connection between theory and data. Additionally, we discuss the statistical procedures employed to obtain constraints on the model parameters. The obtained constraints on the model parameters for all the models are presented in Section V. The performance of the different models is assessed using statistical tools in Section VI. Section VII is dedicated to deriving the relevant quantities that characterize expansion history of the universe based on the model constraints. In Section VIII we provide the concluding remarks for this work. Due to need for careful considerations in solving the modified Friedmann equations, such as avoiding numerical instabilities and minimizing computation time, Appendix A is included to discuss the method used for numerically solving the Friedmann equations. The data for baryonic acoustic oscillations and cosmic chronometer, collected from different sources, are tabulated in Appendix in the Tables III and IV, respectively.

Unless otherwise mentioned we have set $c = 1$ (where, c denotes speed of light in vacuum), and value of the Hubble parameter is expressed in the unit $\text{km s}^{-1}\text{Mpc}^{-1}$.

II. $f(R)$ COSMOLOGY IN METRIC FORMALISM

The $f(R)$ theories of gravity involve generalisation of Lagrangian by making it an arbitrary function of the Ricci scalar R where $f(R) = R$ corresponds to the standard Einstein theory of gravity. Algebraic expressions for $f(R)$, different from $f(R) = R$, define different $f(R)$ -models. The generalized Einstein-Hilbert action for $f(R)$ theories is

$$S = \frac{1}{2\kappa} \int d^4x \sqrt{-g} f(R) + S_m + S_r, \quad (1)$$

where $\kappa = 8\pi G$, g is the determinant of the metric tensor, S_m and S_r are the actions for matter fields and radiation fields, respectively. The variation of this action with respect to the metric gives the corresponding field equation in metric formalism as

$$FR_{\mu\nu} - \frac{1}{2}fg_{\mu\nu} - (\nabla_\mu\nabla_\nu - g_{\mu\nu}\square)F = \kappa T_{\mu\nu}, \quad (2)$$

where $F = \partial f/\partial R$, $\square \equiv g^{\mu\nu}\nabla_\mu\nabla_\nu$ is the covariant D'Alembertian and $T_{\mu\nu}$ is the energy-momentum tensor of matter and radiation. This field equation can also be expressed as

$$FG_{\mu\nu} - F'\nabla_\mu\nabla_\nu R - F''(\nabla_\mu R)(\nabla_\nu R) + g_{\mu\nu} \left[\frac{1}{2}(RF - f) + F'\square R + F''(\nabla R)^2 \right] = \kappa T_{\mu\nu} \quad (3)$$

where $G_{\mu\nu} \equiv R_{\mu\nu} - \frac{1}{2}Rg_{\mu\nu}$ is Einstein tensor and prime(') denotes derivative with respect to R . Taking trace of both sides of Eq. 2 we obtain

$$\square R = \frac{1}{3F'} [\kappa T - 3F''(\nabla R)^2 + 2f - RF], \quad (4)$$

using which in Eq. 3 we rewrite the field equation as

$$G_{\mu\nu} = \frac{1}{F'} \left[F'\nabla_\mu\nabla_\nu R + F''(\nabla_\mu R)(\nabla_\nu R) - \frac{g_{\mu\nu}}{6}(RF + f + 2\kappa T) + \kappa T_{\mu\nu} \right], \quad (5)$$

where $T \equiv T_\mu^\mu$ is the trace of energy-momentum tensor.

In this work we consider the universe to be isotropic and homogeneous at large scale and described by spatially flat Friedmann-Lemaitre-Robertson-Walker (FLRW) metric

$$ds^2 = -dt^2 + a(t)^2 [dr^2 + r^2(d\theta^2 + \sin^2\theta d\phi^2)], \quad (6)$$

where a is the FLRW scale factor. The Hubble parameter(H) is defined as $H \equiv \dot{a}/a$ where we use a generic notation \dot{X} to denote derivative of any quantity X with respect to cosmological time (t). In this formalism, for flat FRLW geometry, the Ricci scalar relates to the Hubble parameter by the relation

$$R = 6(2H^2 + \dot{H}). \quad (7)$$

We consider the content of universe to be a perfect fluid comprising of two components: radiation and matter in the form of pressureless dust (non-relativistic). For the epochs($0 \leq z < 10^4$) when any interaction between matter and radiation could be ignored, the energy-momentum tensor for the fluid can be written as $T_\nu^\mu = \text{diag}(-\rho, p, p, p)$ with $\rho = \rho_m + \rho_r$ and $p = p_r$ (with radiation pressure $p_r = \rho_r/3$), where the subscripts 'm' and 'r' stand for matter and radiation, respectively. Each of the non-interacting components separately follows the continuity equations

$$\dot{\rho}_m + 3H\rho_m = 0, \quad \dot{\rho}_r + 4H\rho_r = 0. \quad (8)$$

The solution to these conservation equations are $\rho_m = \rho_{m0}/a^3$, $\rho_r = \rho_{r0}/a^4$ where subscript '0' denotes values at present epoch.

In the context of the FLRW universe filled with an ideal perfect fluid characterised by ρ and p , Eq. 4 reduces to

$$F'\ddot{R} + F''\dot{R}^2 = - \left[\frac{\kappa(3p - \rho)}{3} + \frac{2f - RF}{3} \right] - 3HF'\dot{R}. \quad (9)$$

using which the '00' and 'ii' components of the field Eq. 5 take following respective forms:

$$-3H^2 = -\frac{1}{F'} \left[\kappa\rho + \frac{RF - f}{2} - 3HF'\dot{R} \right], \quad (10)$$

$$-2\dot{H} = \frac{1}{F'} \left[\kappa(\rho + p) + F''\dot{R}^2 + (\ddot{R} - H\dot{R})F' \right]. \quad (11)$$

The Eqs. 10 and 11 are modified form of the Friedmann equations for $f(R)$ -models. The temporal profile of the Hubble parameter H is commonly expressed in the form $H(z)$, z being the redshift related to the FLRW scale factor by $1 + z = 1/a$ (where, a is normalised to unity at the present epoch). We require this profile of $H(z)$ from the cosmological data sets for obtaining observational constraints on $f(R)$ -models. For this purpose one may solve either the system of: (i) Eqs. 9, 10 and 11 or, (ii) Eqs. 7, 10 and 11. We take the path (ii) to solve the system. Eq. 10 serves as a constraint equation which fixes the initial conditions and must be satisfied at every integration step during the process of finding solutions. Finding analytical solutions is almost impossible, and therefore numerical methods are employed. However, solving this system of ordinary differential equations (ODEs) using a naive approach often leads to numerical instability. Additional details on how to solve this system of ODEs are discussed in Appendix A.

If we compare the modified Friedmann Eqs. 10 and 11 to the usual Friedmann equations with a dark energy component characterised by energy density ρ_{DE} and pressure p_{DE} , *i.e.* with the equations $3H^2 = \kappa(\rho_m + \rho_r + \rho_{\text{DE}})$ and $-2\dot{H} = \kappa(\rho_m + \rho_r + \rho_{\text{DE}} + p_m + p_r + p_{\text{DE}})$, we can deduce the "effective (geometric) dark energy" with density and

pressure corresponding to $f(R)$ -theory as

$$\rho_{\text{DE}} = \frac{1}{\kappa} \left[\frac{RF - f}{2} - 3HF'\dot{R} + 3(1 - F)H^2 \right], \quad (12)$$

and,

$$p_{\text{DE}} = \frac{1}{\kappa} \left[\frac{f - RF}{2} + F'\ddot{R} + 2HF'\dot{R} + F''\dot{R}^2 - (1 - F)(2\dot{H} + 3H^2) \right], \quad (13)$$

with the equation-of-state parameter for this effective dark energy defined as

$$w_{\text{DE}} = \frac{p_{\text{DE}}}{\rho_{\text{DE}}}. \quad (14)$$

Using Eqs. 10 and 11, we may recast Eq. 14 into a more computationally advantageous form (which we use later) as

$$w_{\text{DE}} = \frac{w_{\text{tot}} - \kappa p_{\text{r}}/(3H^2)}{1 - \kappa(\rho_{\text{m}} + \rho_{\text{r}})/(3H^2)}, \quad (15)$$

where

$$w_{\text{tot}} = -1 + \frac{2(1+z)}{3H} \frac{dH}{dz}, \quad (16)$$

and we have taken $p_{\text{m}} = 0$ for the pressureless matter.

The relevant quantities obtained from observations, depending on cosmological models or even through cosmography (a model-independent kinematical approach), indicate that the Universe has recently undergone a transition from a phase of decelerated expansion to accelerated expansion. These quantities include $w_{\text{tot}}|_{z=0} \sim -0.7$, $w_{\text{DE}}|_{z=0} \sim -1$, and a transition redshift (z_t) $\sim 0.5 - 1$. The transition redshift signifies the redshift at which the transition from decelerated to accelerated expansion occurred and is determined by the zero-crossing of the deceleration parameter ($q(z)$) given by

$$q(z) \equiv -\frac{\ddot{a}}{aH^2} = -1 + \frac{(1+z)}{H} \frac{dH}{dz}. \quad (17)$$

In the Λ CDM model, the value of w_{DE} is fixed at -1 for all redshifts due to the presence of the cosmological constant (Λ) term. However, in $f(R)$ models, the source of $w_{\text{DE}}|_{z=0} \sim -1$ arises from the underlying geometry itself. Unlike the Λ CDM model, there is no need to invoke the existence of “dark energy” in $f(R)$ theories of gravity.

III. THE SPECIFIC $f(R)$ MODELS AND THEIR VIABILITY CONDITIONS

In this section we provide a brief introduction to the models examined in this study, both in their originally proposed forms and their subsequent transformations

into more generalized representations. These transformations aim to highlight how these models can be more readily reduced to the Λ CDM model under appropriate conditions. However, before going into the details of each model, it is essential to discuss the viability conditions.

In the metric formalism (unlike Palatini formalism), any viable $f(R)$ cosmological model must satisfy the following set of stringent theoretical conditions (see [27, 28] for detailed discussions):

$$F > 0, \quad \text{for } R \geq R_0 > 0, \quad (18)$$

$$F' > 0, \quad \text{for } R \geq R_0 > 0, \quad (19)$$

$$f(R) \approx R - 2\Lambda, \quad \text{for } R \gg R_0, \quad (20)$$

$$\text{and, } 0 < \frac{RF'}{F}(r) < 1 \quad \text{at } r = -\frac{RF}{f} = -2, \quad (21)$$

where R_0 denotes the Ricci scalar at the present epoch.

These conditions arise from various considerations. Firstly, the effective gravitational constant ($G_{\text{eff}} = G/F$) must be positive, ensuring the avoidance of anti-gravity (as expressed in Eq. 18). Besides, any acceptable $f(R)$ -model should exhibit stability under perturbations and avoid the instability of Dolgov-Kawasaki type (Eq. 19). Similar to the Λ CDM model, a viable $f(R)$ model must also be consistent with local gravity tests (Eqs. 19 and 20). Furthermore, the existence of a matter-dominated epoch in cosmological dynamics necessitates that an $f(R)$ model satisfies the conditions given by Eqs 19 and 20. Lastly, Eq. 20 ensures the stability of the late-time de-Sitter solution, from which the late-time accelerated expansion of the Universe is usually inferred.

The viability conditions mentioned above can be more easily assessed for an $f(R)$ -model if we can somehow transform that model into the following form:

$$f(R) = R - 2\Lambda y(R, b, \Lambda), \quad (22)$$

where the function $y(R, b, \Lambda)$ serves to measure the deviation from the Λ CDM model, with the parameter b (referred to as the “distortion/deviation parameter”) specifically quantifying the extent of the deviation [17]. For this reason, all the models examined in this study are recast into the form of Eq. 22, allowing for a clearer evaluation of their compliance with the viability conditions.

More specifically, the viability conditions in Eqs. 19 and 20 can be alternatively written as $\lim_{R \rightarrow \infty} f(R) = R + C_0$, where C_0 represents a constant value. In order for a candidate $f(R)$ -model to exhibit asymptotic behavior similar to the standard Λ CDM model (which is supported by observations of the cosmic microwave background), we can identify that $C_0 = -2\Lambda$, where Λ corresponds to the cosmological constant introduced by Einstein and Hilbert in their action. This amounts to writing symbolically $\Lambda^\Lambda = \Lambda^{f(R)}$ where the superscripts

Λ and $f(R)$ denote quantities in reference to the Λ CDM model and any viable $f(R)$ -model, respectively. This relation may also be written as

$$\Omega_{\Lambda,0}^\Lambda (H_0^\Lambda)^2 = \Omega_{\Lambda,0}^{f(R)} (H_0^{f(R)})^2, \quad (23)$$

where subscript ‘0’ denotes values at present time. Furthermore, considering the definition of the energy-momentum tensor and the resulting conservation equation (Eq. 8), we can infer that both the Λ CDM model and any viable $f(R)$ -model yield identical matter density and radiation density at the current epoch *i.e.*

$$\Omega_{i,0}^\Lambda (H_0^\Lambda)^2 = \Omega_{i,0}^{f(R)} (H_0^{f(R)})^2 = \frac{8\pi G}{3} \rho_{i,0}, \quad (24)$$

where the subscript $i = (m, r)$ stands for (matter, radiation). Also any viable $f(R)$ -model is expected to exhibit deviations from the standard Λ CDM model predominantly during the late times, in order that the explanation for accelerated expansion at present epoch comes from vanishing Λ . In general terms, this implies

$$\Omega_{i,0}^\Lambda \neq \Omega_{i,0}^{f(R)}, \quad H_0^\Lambda \neq H_0^{f(R)}. \quad (25)$$

Based on Eqs. 23-25 and the initial condition requirements for solving the ODE system described in Eqs. 7, 10, and 11 (see Appendix A), we utilize parameters $(\Omega_{m,0}^\Lambda, b, H_0^\Lambda)$ for model-fitting to the data. However, while reporting our findings, we express the results in terms of the parameters $(\Omega_{m,0}^{f(R)}, b, H_0^{f(R)})$, which are determined using Eq. 24.

A. The Hu-Sawicki Model

The Hu-Sawicki model, initially proposed in [29], is described by the following equation:

$$f(R)_{\text{HS}} = R - \mu^2 \frac{c_1 (R/\mu^2)^{n_{\text{HS}}}}{1 + c_2 (R/\mu^2)^{n_{\text{HS}}}}, \quad (26)$$

where c_1 and c_2 are dimensionless parameters, n_{HS} is a positive constant typically assumed to be an integer, and $\mu^2 \approx \Omega_{m,0} H_0^2$. By defining $\mu^2 c_1 / 2c_2 \equiv \Lambda$ and $2 \left(c_2^{1-1/n_{\text{HS}}} \right) / c_1 \equiv b$, we can express Eq. 26 as [17]:

$$f(R)_{\text{HS}} = R - 2\Lambda \left[1 - \left\{ 1 + \left(\frac{R}{b\Lambda} \right)^{n_{\text{HS}}} \right\}^{-1} \right]. \quad (27)$$

We identify the parameter Λ as the usual cosmological constant, and b as the deviation parameter, which indicates the model’s deviation from the Λ CDM model. In order to satisfy the viability conditions $F > 0$ and $F' > 0$ for $R \geq R_0$, it is necessary to consider $b > 0$ (especially when n_{HS} is an odd integer). Although many researchers have constrained the scenarios where $n_{\text{HS}} = 1$ and/or 2 [17, 18, 21, 22, 24–26], they have acknowledged computational challenges as a hindrance to explore the case of $n_{\text{HS}} = 3$ (further elaboration on this point is provided in Sec. V). In this investigation, we have also imposed constraints on the case $n_{\text{HS}} = 3$.

B. The Starobinsky Model

The model proposed by Starobinsky [30] is

$$f(R)_{\text{ST}} = R - \lambda R_S \left[1 - \left(1 + \frac{R^2}{R_S^2} \right)^{-n_s} \right], \quad (28)$$

where n_s is a positive constant, $\lambda (> 0)$ and $R_S \approx R_0$ are free parameters (where R_0 denotes the Ricci scalar at present epoch). This model too can be reformulated in a more general form as [17]

$$f(R)_{\text{ST}} = R - 2\Lambda \left[1 - \left\{ 1 + \left(\frac{R}{b\Lambda} \right)^2 \right\}^{-n_s} \right] \quad (29)$$

with $\Lambda = \lambda R_S / 2$ and $b = 2/\lambda$. In this study, we have imposed constraints on the cases where $n_s = 1$ and the reason for not exploring higher values of n_s is explained later in Sec. V. Note that the Hu-Sawicki model (Eq. 27) with $n_{\text{HS}} = 2$ and the Starobinsky model (Eq. 29) with $n_s = 1$ are equivalent. Unlike the Hu-Sawicki model (with $n_{\text{HS}} = 1$), the viability condition for the Starobinsky model does not require $b > 0$. Based on the algebraic form of the Starobinsky model (Eq. 29), we can infer that regardless of the data used, the parameter b must exhibit a symmetric distribution (centered around $b = 0$) from the MCMC fitting procedure. Since our interest lies in investigating deviations from the Λ CDM model supported by the data, we considered $b > 0$ without loss of generality.

C. The Exponential Model

The exponential model, initially proposed as a viable $f(R)$ model in [31], has been further investigated in [19, 25, 32, 33] (also see references therein), is given by

$$f(R)_{\text{E}} = R + \alpha [\exp(-\beta R) - 1], \quad (30)$$

where α and β are the parameters of this model. For large R , an acceptable $f(R)$ -model must approximately resemble the Λ CDM, which is achievable only when $\alpha > 0$ and $\beta > 0$. By substituting $\Lambda = \alpha/2$ and $b = 2/(\alpha\beta)$ the exponential model can be expressed as

$$f(R)_{\text{E}} = R - 2\Lambda \left[1 - \exp\left(-\frac{R}{b\Lambda}\right) \right], \quad (31)$$

from where it becomes evident that when R becomes significantly larger than $b\Lambda$ ($R \gg b\Lambda$), the function $f(R)_{\text{E}}$ approaches $R - 2\Lambda$.

D. The Tsujikawa Model

Tsujikawa proposed an alternative model [34] as

$$f(R)_{\text{T}} = R - \xi R_{\text{T}} \tanh\left(\frac{R}{R_{\text{T}}}\right), \quad (32)$$

where $\xi(> 0)$ and $R_T(> 0)$ are the model parameters. With $\Lambda = \xi R_T/2$ and $b = 2/\xi$, the model can be rewritten as

$$f(R)_T = R - 2\Lambda \tanh\left(\frac{R}{b\Lambda}\right). \quad (33)$$

We see clearly that when the parameter $b \rightarrow 0$ (which corresponds to $\xi \rightarrow \infty$, $R_T \rightarrow 0$, while ξR_T remains finite), the model reduces to $f(R)_T = R - 2\Lambda$.

E. The ArcTanh Model

In this study we also examined a model proposed in [20] as

$$f(R)_{\text{aTanh}} = R - \frac{2\Lambda}{1 + b \arctanh\left(\frac{\Lambda}{R}\right)}, \quad (34)$$

where the parameter b is required to be positive, in order to prevent any occurrence of future singularities.

IV. OBSERVED COSMOLOGICAL DATA

In this section we present a concise overview of the cosmological data sets utilized in this study. For any given $f(R)$ model, the system of Eqs. 7, 10 and 11 is solved, primarily yielding the function $H(z)$. So, it becomes necessary to outline the theoretical equations connecting $H(z)$ with various observed quantities. Additionally, at the end of this section, a brief introduction is provided on the statistical techniques employed to extract model parameters from the data.

A. Type Ia Supernova Data

Type Ia Supernovae (SNIa), known as standard candles [35], have significantly contributed to our comprehension of cosmology. The SNIa observations [2, 4] played a pivotal role in the discovery of the accelerated expansion of the present-day universe. In this study we used the apparent magnitude data for SNIa obtained from the recently released PantheonPlus compilation [36]. This compilation comprises of 1701 distinct light curves of 1550 unique spectroscopically confirmed SNIa, sourced from 18 surveys. This compilation provides SNIa data within the range $0.00122 < z_{\text{HD}} < 2.26137$, where z_{HD} denotes the Hubble diagram redshift. It offers a considerably larger number of low-redshift data compared to the previous Pantheon compilation [37]. In our current work, we employ the apparent magnitude at maximum brightness (m_b), heliocentric redshift (z_{hel}), cosmic microwave background corrected redshift (z_{cmb}), and the total (statistical + systematic) covariance matrix from this compilation [36].

The theoretical definition of the apparent magnitude involves the luminosity distance, which is given by the integral expression:

$$d_L(z) = c(1 + z_{\text{hel}}) \int_0^{z_{\text{cmb}}} \frac{dz'}{H(z')}, \quad (35)$$

where the function $H(z)$ is obtained by solving the system of Eqs. 7, 10 and 11. The apparent magnitude is defined as

$$m_{\text{th}} = M + 5 \log_{10}\left(\frac{c/H_0}{\text{Mpc}}\right) + 5 \log_{10}(D_L(z)) + 25, \quad (36)$$

where M represents the absolute magnitude, and $D_L(z) \equiv H_0 d_L(z)/c$ is the dimensionless Hubble-free luminosity distance. The computation of apparent magnitude involves a degeneracy between the absolute magnitude (M) and the Hubble parameter at the current epoch (H_0), as evident from the Eq. 36. Therefore, after marginalizing over these nuisance parameters (M and H_0), the appropriate residual that needs to be minimized for model fitting is given by [38]

$$\tilde{\chi}_{\text{sn}}^2 = A - \frac{B^2}{D} + \log \frac{D}{2\pi}, \quad (37)$$

where $A = (m_b - m_{\text{th}})^T C^{-1} (m_b - m_{\text{th}})$, $B = (m_b - m_{\text{th}})^T C^{-1} \mathbf{1}$, and $D = \mathbf{1}^T C^{-1} \mathbf{1}$ and C represents the total covariance matrix of the data (provided in the Pantheon+ compilation). $\mathbf{1}$ is an array of ones of length equal to the number of data points.

B. Cosmic Chronometers Data

By examining the differential age evolution [39–41] of old elliptical galaxies, where star formation and interactions with other galaxies have ceased, previous studies have provided 32 data points for $H(z)$ in the redshift range of 0.07–1.965 [41–48] (compiled in the Table IV of the Appendix). This so called differential age method, employed in these studies, uses the relation

$$H(z) = -\frac{1}{1+z} \frac{dz}{dt} \simeq -\frac{1}{1+z} \frac{\Delta z}{\Delta t}, \quad (38)$$

to obtain $H(z)$. The parameters of any model are estimated by minimizing the following residual:

$$\chi_{\text{CC}}^2 = \sum_{i=1}^{32} \frac{(H_{\text{obs}}(z_i) - H_{\text{th}}(z_i))^2}{\sigma_{H,i}^2}, \quad (39)$$

where $H_{\text{obs}}(z_i)$'s are the observed values of the Hubble parameter function at redshift z_i , while $\sigma_{H,i}^2$ denotes the corresponding uncertainties associated with the measurements of $H_{\text{obs}}(z_i)$. The theoretical Hubble function at redshift z_i , which is model-dependent and obtained from the solutions of Eqs. 7, 10, and 11, is denoted by $H_{\text{th}}(z_i)$ in the above Eq. 39.

C. BAO Data

In the Big Bang Model of the universe, prior to decoupling of matter and radiation components, the contents of the Universe were evenly distributed, albeit with small fluctuations. Photons and baryons were strongly coupled through Thomson scattering. As the universe expanded and cooled, resulting in a decrease in temperature and density, the fluctuations were amplified by gravity. The gravitational pull caused the tightly bound photon-baryon mixture to condense in regions with higher densities, resulting in compressions and rarefactions in the form of acoustic waves known as Baryonic Acoustic Oscillations (BAO). Matter and radiation were then decoupled and this epoch which is marked by the release of baryons from the Compton drag of photons is known as drag epoch (z_d), after which the photons travelled freely, whereas acoustic waves remained frozen in the baryons. The length scale characterizing the maximum distance traveled by the acoustic wave before decoupling is known as sound horizon at the epoch of drag (r_d). BAO, therefore, holds the status of standard ruler for length scale in Cosmology [49, 50].

We have compiled a collection of 30 data points representing various BAO observables from a range of surveys, as documented in the literature [51–70]. These data points, which are used in our current study, are listed in the Table III (in the Appendix). In our calculations for the drag epoch z_d and the sound horizon at the epoch of drag r_d , we employ improved fits from [71]. The BAO observables include the Hubble distance, which is defined as $D_H = c/H(z)$, the transverse comoving distance ($D_M(z)$), the angular diameter distance ($D_A(z)$), and the volume-averaged distance ($D_V(z)$) which are defined as

$$D_A(z) = \frac{c}{1+z} \int_0^z \frac{dz'}{H(z')}, \quad (40)$$

$$D_M(z) = (1+z)D_A(z), \quad (41)$$

and,

$$D_V(z) = \left[(1+z)^2 D_A^2(z) \frac{z}{H(z)} \right]^{1/3}. \quad (42)$$

Once again $H(z)$ in the above relations is obtained by solving Eqs. 7, 10, and 11.

For fitting any model to the uncorrelated data points of the BAO data, the following residual has been used

$$\chi_{\text{BAO-UC}}^2 = \sum_{i=1}^{20} \left[\frac{A_{\text{th}}(z_i) - A_{\text{obs}}(z_i)}{\sigma_i} \right]^2, \quad (43)$$

where $A_{\text{obs}}(z_i)$ and σ_i respectively denote the observed values and their uncertainties at redshift z_i and A_{th} denotes the theoretical prediction from model under consideration. These quantities are given in the columns 2-4 of the Table III. For correlated data points the appropriate residual to be minimized is

$$\chi_{\text{BAO-C}}^2 = \sum_{j=1}^4 \left[(\mathbf{A}_{\text{th}} - \mathbf{A}_{\text{obs}})_j^T \mathbf{C}_j^{-1} (\mathbf{A}_{\text{th}} - \mathbf{A}_{\text{obs}})_j \right], \quad (44)$$

where \mathbf{C}_j 's are the covariance matrices of the 4 different data-sets and $(\mathbf{A}_{\text{th}} - \mathbf{A}_{\text{obs}})_j$ denotes an array of difference between observed and theoretical values for each of the 4 data-sets. These data and the covariance matrix can be found from the corresponding source papers referred in the last column of Table III. For the whole data-set of BAO, the χ^2 which is to be minimized is

$$\chi_{\text{BAO}}^2 = \chi_{\text{BAO-UC}}^2 + \chi_{\text{BAO-C}}^2. \quad (45)$$

D. H II starburst Galaxies Data

HII galaxies (HIIG) are massive and compact starburst structures surrounded by ionized hydrogen gas. Their optical emission spectra exhibit strong and narrow Balmer $H\alpha$ and $H\beta$ lines, along with a weak continuum. The cosmological significance of HIIG observation comes from the empirically established correlation between the luminosity (L) of the $H\beta$ lines and the velocity dispersion (σ , which is a measure of the width of the spectral lines). This correlation is attributed to the fact that an increase in the mass of the starburst component leads to a simultaneous increase in the number of ionized photons (and thus the luminosity L) and the turbulent velocity (hence, the velocity dispersion σ) (see [72] and references therein).

In this study, we have used a total of 181 data points from [72–76] corresponding to the emission of the Balmer $H\beta$ line. These data points span a redshift range of $0.0088 < z < 2.5449$. It is important to note that the redshift coverage provided by the latest SNIa data is as follows: we have 8 data points for $z_{\text{SN}} > 1.4$, while for $z_{\text{HIIG}} > 1.4$ we have 69 data points, and for $z_{\text{HIIG}} > z_{\text{SN,max}}$ we have 11 observations of HIIG. Consequently, the observations of HIIG not only explore hitherto unexplored higher redshift regions compared to SNIa but also provide a denser coverage of these higher redshift regions in comparison to SNIa.

The empirical relation between the luminosity L and the dispersion of velocity σ is given by

$$\log \left[\frac{L}{\text{erg/s}} \right] = \beta \log \left[\frac{\sigma}{\text{km/s}} \right] + \alpha, \quad (46)$$

where we take $\beta = 5.022 \pm 0.058$ and $\alpha = 33.268 \pm 0.083$ from [72, 76]. From the luminosity distance of HIIG,

$d_L = [L/(4\pi F)]^{1/2}$, we can derive the distance modulus as

$$\mu_o = 2.5 \left(\alpha + \beta \log \left[\frac{\sigma}{\text{km/s}} \right] - \log \left[\frac{\sigma}{\text{erg/s/cm}^2} \right] - 40.08 \right). \quad (47)$$

Using Eq. 47, we compute the distance moduli of HII G from the observables L , σ , and F . For any given cosmological model with theoretical distance moduli μ_θ (represented as $m_{\text{th}} - M$ in Eq. 36), the parameters associated with that model can be constrained by minimising the following χ^2 function

$$\chi_{\text{HII G}}^2 = \sum_{i=1}^{181} \frac{[\mu_o - \mu_\theta]^2}{\epsilon^2}, \quad (48)$$

where

$$\epsilon^2 = \epsilon_{\mu_o, \text{stat}}^2 + \epsilon_{\mu_\theta, \text{stat}}^2 + \epsilon_{\text{sys}}^2, \quad (49)$$

with

$$\epsilon_{\mu_o, \text{stat}}^2 = 6.25 (\epsilon_{\log F}^2 + \beta^2 \epsilon_{\log \sigma}^2 + \epsilon_\beta^2 (\log \sigma)^2 + \epsilon_\alpha^2), \quad (50)$$

$$\epsilon_{\mu_\theta, \text{stat}}^2 = \left[\frac{5}{\ln 10} \left(\frac{c(1+z)}{d_L(z)H(z)} + \frac{1}{1+z} \right) \sigma_z \right]^2, \quad (51)$$

and $\epsilon_{\text{sys}} = 0.0257$ as suggested in [72, 76, 77]. The uncertainty contribution of $\epsilon_{\mu_\theta, \text{stat}}$ in the distance modulus is due to the uncertainties in redshifts ($\sigma_z \sim 10^{-4}$) of HII G and is derived from simple error propagation theory.

E. Local Measurement of H_0

A contentious issue remains regarding the current value of the Hubble parameter H_0 . The Planck constraints provide a value of $H_0 = 67.4 \pm 0.5$ [78], while the locally measured value by the SH0ES collaboration yields $H_0 = 73.04 \pm 1.04$ [79]. The discrepancy between these two measurements, known as the Hubble tension, is significant at the $4 - 5\sigma$ level. To address this tension, we have included in our study both scenarios - with vis-a-vis without the SH0ES prior for H_0 . The contribution of this data point to the total χ^2 is given by

$$\chi_{\text{SH0ES}}^2 = \frac{(H_0 - 73.04)^2}{1.04^2}. \quad (52)$$

F. Methodology

We employed the well-known Markov Chain Monte Carlo (MCMC) analysis for parameter estimations of the models. This involves maximizing the likelihood function, given by

$$\mathcal{L} = \exp \left(- \sum_i \chi_i^2 / 2 \right), \quad (53)$$

where the subscript ‘ i ’, depending on the combination of different data-sets used, stands for one or more from the set: { ‘SN’, ‘CC’, ‘BAO’, ‘HII G’, ‘SH0ES’ }. These χ_i^2 ’s are defined in Eqs. 37, 39, 45, 48 and 52. To get posterior probability distribution of the model parameters we also need to set priors on them. For the reasons mentioned in the last section and will further be discussed in the Appendix A, for all the $f(R)$ models in this work we do data-fitting in terms of the parameters: $(\Omega_{\text{m}0}^\Lambda, b, H_0^\Lambda)$. We used the uniform priors $\Omega_{\text{m}0}^\Lambda \in [0, 1]$ and $H_0^\Lambda \in [50, 90]$ for all the models, whereas priors for b require further considerations. From the algebraic expressions of these six $f(R)$ -models we worked out and established a hierarchy of similarity of these models with the standard Λ CDM model using some ‘measures-of-similarity’ (e.g. mean-square-error, correlation, dynamic time warping *etc.*). A ballpark hierarchy of similarity we find is: the most similar $f(R)$ models are the Tsujikawa model (TSUJI) and the Hu-Sawicki model ($n_{\text{HS}} = 3$) (HS3), followed by the Starobinsky ($n_s = 1$) (ST1) and the exponential (EXP) models, and the least similar ones are the Hu-Sawicki model ($n_{\text{HS}} = 1$) (HS1) and the arcTanh (aTanh) models. To allow for the exploration that whether the data supports a model different from the Λ CDM model, an $f(R)$ model which is more similar to the Λ CDM requires a bigger change in b to make them noticeably different from the Λ CDM model. Consequently we use uniform priors $b \in [0, b_{\text{max}}]$ where b_{max} is 7, 7, 5, 5, 3 and 3 for the models HS3, TSUJI, ST1, EXP, HS1 and aTanh, respectively.

We developed our own PYTHON codes using the publicly available PYTHON modules: (i) for solving stiff ODEs [80], (ii) to perform MCMC analysis — EMCEE [81], and (iii) for plotting of posterior probability distributions of the parameters — GetDist [82].

V. RESULTS: OBSERVATIONAL CONSTRAINTS ON $f(R)$ MODELS

In this section we will discuss our findings regarding the parameters of the six $f(R)$ models and the Λ CDM model. We have considered five combinations of data sets: SNIa+CC (SC), SNIa+BAO+CC (SBC), SNIa+CC+HII G (SCHII), BAO+CC+HII G (BCHII), and SNIa+BAO+CC+HII G (SBCHII). We also separately included a SH0ES prior for the Hubble parameter H_0 for each of these combinations. While each data set individually can constrain any model, they may not necessarily provide tight constraints on the parameters. The choice of data combinations is also guided by considerations of goodness-of-fit.

Acronym and Color convention: In addition to the above mentioned acronyms for different data sets, when including the SH0ES prior for H_0 , we append the notations as follows: SCH_0 to denote SNIa+CC+ H_0 and $\text{SC}(H_0)$ to denote SNIa+CC or SNIa+CC+ H_0 , depend-

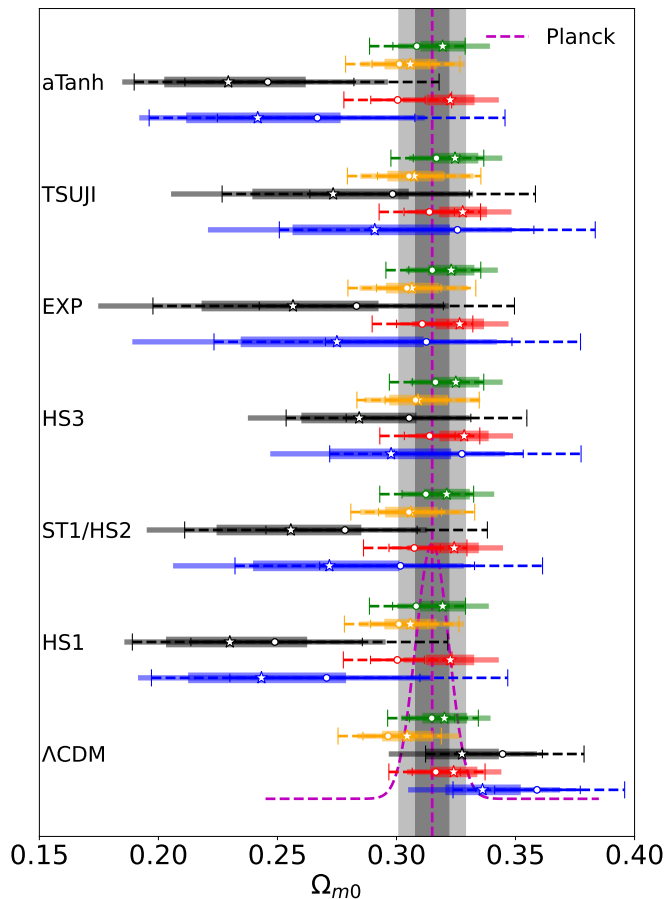


FIG. 1. This figure is helpful in getting a sense of variations of Ω_{m0} from model to model and with data for a given model. Different colors represent different data-set combinations and these are same as in any of the parameter distribution plots(e.g. Fig. 6) or see 2nd paragraph of Sec.V. The blank star and blank circle markers represent median values for the cases with and without SH0ES prior for H_0 , respectively. The thick and thin horizontal colored bars represent 1-sigma(68.26%) and 2-sigma(95.44%) confidence intervals for the cases with SH0ES prior. The colored continuous/dashed lines represent 1-sigma(68.26%, with smaller cap size) and 2-sigma(95.44%, with bigger cap size) confidence intervals for the cases without SH0ES prior.

ing on the case. Similar notations are used for the other four data sets. Unless otherwise specified, the following color and data set correspondences are used in the upcoming figures: (i) $SC(H_0)$ —Blue, (ii) $SBC(H_0)$ —Red, (iii) $SCHII(H_0)$ —Black, (iv) $BCHII(H_0)$ —Orange, and (v) $SBCHII(H_0)$ —Green.

We generated MCMC samples of size 875,000 (with 25 walkers, each taking 35,000 steps) for each parameter in all the cases, where a case refers to a specific combination of a given model and a data set. These raw MCMC sample chains underwent tests for convergence and independence. To ensure convergence, an initial portion of the chain was discarded to obtain a “burned chain.” We

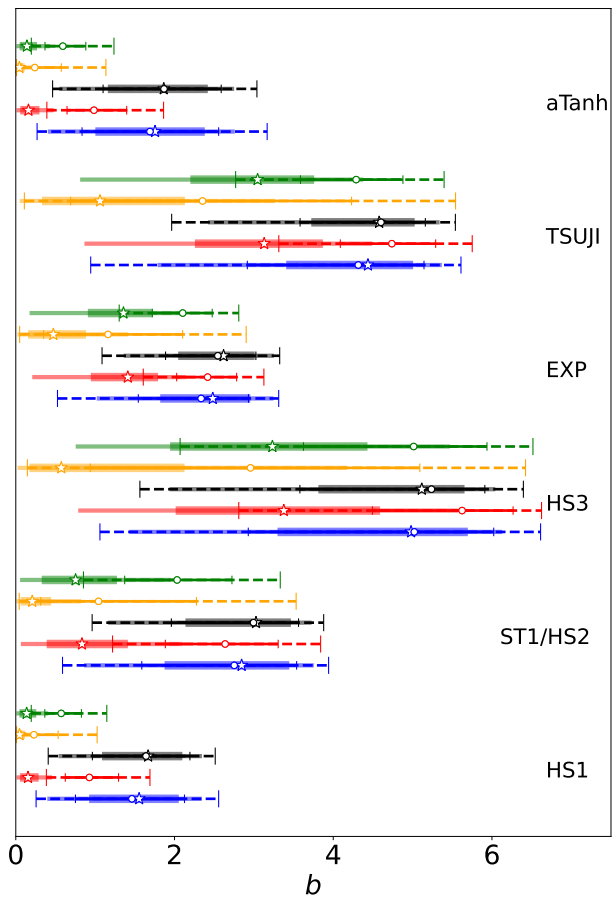


FIG. 2. This figure is helpful in getting a sense of variations of the deviation parameter b from model to model and with data for a given model. Different colors represent different data-set combinations and these are same as in any of the parameter distribution plots(e.g. Fig. 6) or see 2nd paragraph of Sec.V. The blank star and blank circle markers represent median values for the cases with and without SH0ES prior for H_0 , respectively. The thick and thin horizontal colored bars represent 1-sigma(68.26%) and 2-sigma(95.44%) confidence intervals for the cases with SH0ES prior. The colored continuous/dashed lines represent 1-sigma(68.26%, with smaller cap size) and 2-sigma(95.44%, with bigger cap size) confidence intervals for the cases without SH0ES prior.

removed the first 125,000 steps (i.e., 5,000 initial steps of each walkers) to obtain the burned chain. In order to have independent and uncorrelated samples, the burned chains needed to be properly thinned. We thinned the burned chains by a factor of 0.75 times the integrated auto-correlation time. As a result, depending on the case, we obtained convergent and independent samples of varying sizes, approximately ranging from 15,000 to 20,000. All the statistical inferences about the model parameters were then obtained from these burned and thinned subsamples.

The median values of model parameters and 1-sigma confidence intervals on them are presented in the Tables I and II. The Figs 4-17 display 2D contour plots depict-

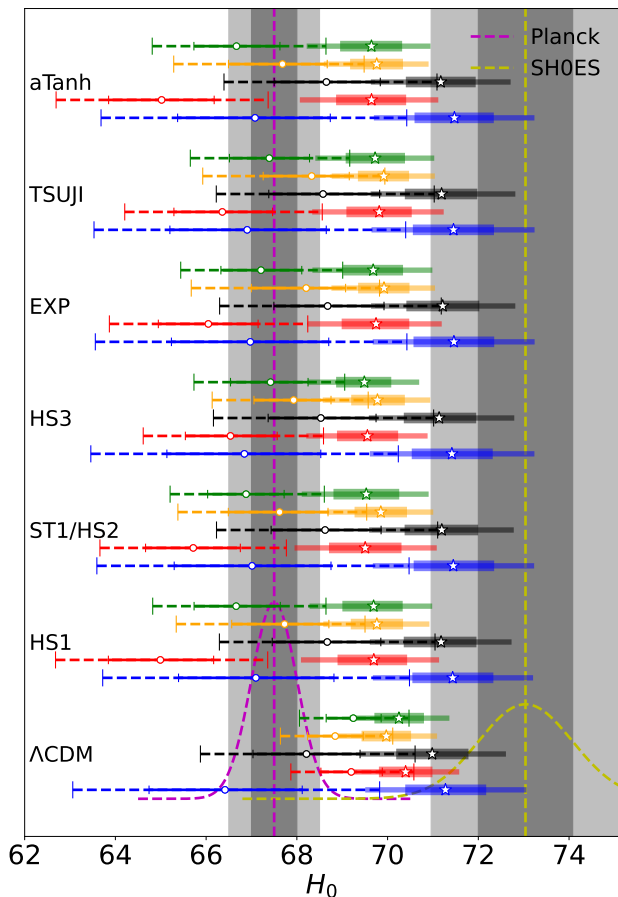


FIG. 3. Hubble Tension: Different colors represent different data-set combinations and these are same as in any of the parameter distribution plots (e.g. Fig. 6) or see 2nd paragraph of Sec.V. The blank star and blank circle markers represent median values for the cases with and without SH0ES prior for H_0 , respectively. The thick and thin horizontal colored bars represent 1-sigma(68.26%) and 2-sigma(95.44%) confidence intervals for the cases with SH0ES prior. The colored continuous/dashed lines represent 1-sigma(68.26%, with smaller cap size) and 2-sigma(95.44%, with bigger cap size) confidence intervals for the cases without SH0ES prior.

ing the posterior probability distribution of the parameters, which provide an indication of potential correlations among the parameters, as well as 1D marginalised distributions of each parameter are also shown there.

Before getting into the detailed results for individual models, we would like to highlight some overall observations regarding the model parameters in the light of Figs. 1, 2, and 3. (i) Ω_{m0} : For all models and data-set combinations, either the median values of Ω_{m0} fall within the 1-2 sigma interval of the Planck value ($\Omega_{m0,Planck} = 0.315 \pm 0.007$ [78]) or, the Planck value is within the 1-2 sigma intervals of the model's median values of Ω_{m0} (for cases with or without the SH0ES prior for H_0). (ii) b : There is a general trend of a shift towards lower values of b when considering the

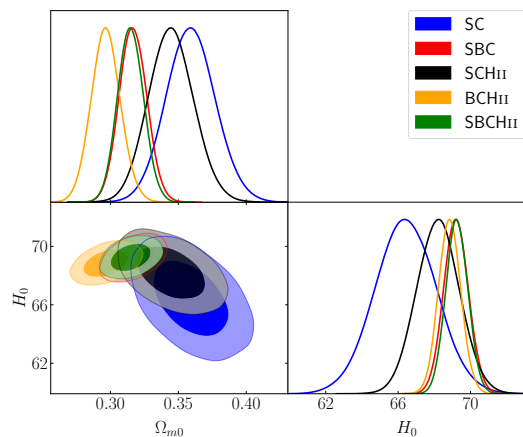


FIG. 4. The Λ CDM Model (without SH0ES prior for H_0): The posterior probability distribution plots of fitted parameters. The color correspondence for different data-set combinations can be seen in the figure legends. The darker and lighter shades of colors represent 1-sigma(68.26%) and 2-sigma(95.44%) confidence intervals, respectively.

SH0ES prior for H_0 compared to the corresponding cases without the SH0ES prior for the SBC(H_0), BCHII(H_0), and SBCHII(H_0) data-sets, whereas opposite trends are observed for the SC(H_0) and SCHII(H_0) data-sets. (iii) H_0 : Without the SH0ES prior for H_0 , for all models and data-set combinations, either the median values of H_0 are within a 1-2 sigma interval of the Planck value ($H_{0,Planck} = 67.4 \pm 0.5$ [78]) or, the Planck value is within a 1-2 sigma interval of the model's median values of H_0 . However, with the SH0ES prior for H_0 , there are slight departures towards higher values of H_0 (as expected), but they are not close to $H_{0,SH0ES} = 73.04 \pm 1.04$ [79]. It is worth noting that the cases with the SH0ES prior for H_0 generally have tighter bounds on the model's H_0 values (this observation does not hold true for Ω_{m0} or b). Additionally, there is less overall tension among the model-fitted values of H_0 compared to the tension between $H_{0,Planck}$ and $H_{0,SH0ES}$.

A. Constraints on Λ CDM Model

We have also included the results for the Λ CDM model, which is commonly used as a benchmark for assessing $f(R)$ models. We consider a two-parameter Λ CDM model, with the Hubble parameter given by $H = H_0 \sqrt{\Omega_{m0}(1+z)^3 + (1 - \Omega_{m0})}$, where the two parameters Ω_{m0} and H_0 stand for the matter density and the Hubble parameter at the present epoch, respectively. The median values along with 1-sigma confidence intervals for these parameters are presented in Tables I and II. The posterior probability distribution of Ω_{m0} and H_0 , both for the respective cases - without and with the SH0ES prior for H_0 - are depicted in Figs 4 and

TABLE I. Results from the MCMC fitting process(for the cases without SH0ES prior for H_0): The median values of the model parameters along with 1-sigma(68.26%) confidence intervals on them, the transition redshift(z_t), the current values of EoS parameter for geometric/dark energy component(w_{DE0}) and total EoS parameter(w_{tot0}), the minimum values of χ^2 and other quantities for making statistical inferences such as the reduced chi-square value $\chi_{\text{red}}^2 = \chi_{\text{min}}^2/\nu$ (where the number of degrees of freedom $\nu = N - k$, N is the total number of data points and k is the number of model parameters), the Akaike Information Criterion(AIC), the Bayesian Information Criterion(BIC), $\Delta\text{AIC} = \text{AIC}_{f(R)\text{ model}} - \text{AIC}_{\Lambda\text{CDM model}}$ and $\Delta\text{BIC} = \text{BIC}_{f(R)\text{ model}} - \text{BIC}_{\Lambda\text{CDM model}}$ — for all the models and data set combinations considered in this work.

Data	Ω_{m0}	b	H_0	z_t	w_{DE0}	w_{tot0}	χ^2	χ_{red}^2	AIC	BIC	ΔAIC	ΔBIC
ACDM												
SC	$0.36^{+0.018}_{-0.018}$	—	$66.42^{+1.703}_{-1.674}$	$0.53^{+0.040}_{-0.039}$	-1	$-0.64^{+0.018}_{-0.018}$	1777.31	1.03	1781.31	1792.22	0.0	0.0
SBC	$0.32^{+0.010}_{-0.010}$	—	$69.20^{+0.684}_{-0.669}$	$0.63^{+0.025}_{-0.025}$	-1	$-0.68^{+0.010}_{-0.010}$	1815.39	1.03	1819.39	1830.34	0.0	0.0
SCHII	$0.34^{+0.017}_{-0.016}$	—	$68.21^{+1.182}_{-1.179}$	$0.56^{+0.039}_{-0.037}$	-1	$-0.66^{+0.017}_{-0.016}$	2145.62	1.12	2149.62	2160.73	0.0	0.0
BCHII	$0.30^{+0.011}_{-0.011}$	—	$68.85^{+0.619}_{-0.608}$	$0.68^{+0.029}_{-0.029}$	-1	$-0.70^{+0.011}_{-0.011}$	408.22	1.69	412.22	419.19	0.0	0.0
SBCHII	$0.31^{+0.010}_{-0.009}$	—	$69.24^{+0.613}_{-0.599}$	$0.63^{+0.024}_{-0.024}$	-1	$-0.69^{+0.010}_{-0.009}$	2180.25	1.12	2184.25	2195.39	0.0	0.0
HS1												
SC	$0.27^{+0.039}_{-0.041}$	$1.46^{+0.662}_{-0.711}$	$67.10^{+1.721}_{-1.704}$	$0.78^{+0.188}_{-0.132}$	$-0.78^{+0.070}_{-0.078}$	$-0.57^{+0.031}_{-0.033}$	1773.75	1.03	1779.75	1796.11	-1.56	3.9
SBC	$0.30^{+0.011}_{-0.011}$	$0.93^{+0.368}_{-0.303}$	$64.99^{+1.175}_{-1.145}$	$0.68^{+0.037}_{-0.035}$	$-0.84^{+0.040}_{-0.041}$	$-0.59^{+0.027}_{-0.027}$	1800.65	1.02	1806.65	1823.07	-12.74	-7.26
SCHII	$0.25^{+0.037}_{-0.035}$	$1.64^{+0.553}_{-0.676}$	$68.67^{+1.181}_{-1.213}$	$0.87^{+0.188}_{-0.145}$	$-0.77^{+0.061}_{-0.071}$	$-0.57^{+0.029}_{-0.031}$	2139.44	1.12	2145.44	2162.1	-4.18	1.37
BCHII	$0.30^{+0.012}_{-0.012}$	$0.23^{+0.305}_{-0.161}$	$67.73^{+0.977}_{-1.165}$	$0.67^{+0.032}_{-0.033}$	$-0.96^{+0.065}_{-0.032}$	$-0.67^{+0.050}_{-0.028}$	408.19	1.7	414.19	424.64	1.97	5.44
SBCHII	$0.31^{+0.010}_{-0.010}$	$0.57^{+0.255}_{-0.206}$	$66.66^{+0.973}_{-0.927}$	$0.65^{+0.030}_{-0.029}$	$-0.89^{+0.037}_{-0.039}$	$-0.61^{+0.026}_{-0.027}$	2171.26	1.12	2177.26	2193.97	-6.99	-1.42
ST1/HS2												
SC	$0.30^{+0.031}_{-0.034}$	$2.75^{+0.786}_{-1.165}$	$67.01^{+1.740}_{-1.716}$	$0.75^{+0.155}_{-0.118}$	$-0.81^{+0.085}_{-0.071}$	$-0.56^{+0.042}_{-0.035}$	1773.24	1.02	1779.24	1795.61	-2.07	3.39
SBC	$0.31^{+0.011}_{-0.011}$	$2.64^{+0.668}_{-0.754}$	$65.72^{+1.038}_{-1.052}$	$0.72^{+0.042}_{-0.040}$	$-0.82^{+0.047}_{-0.043}$	$-0.57^{+0.032}_{-0.030}$	1799.22	1.02	1805.22	1821.64	-14.17	-8.7
SCHII	$0.28^{+0.030}_{-0.033}$	$2.99^{+0.568}_{-1.035}$	$68.62^{+1.234}_{-1.190}$	$0.84^{+0.169}_{-0.132}$	$-0.78^{+0.087}_{-0.074}$	$-0.56^{+0.046}_{-0.038}$	2138.76	1.12	2144.76	2161.43	-4.86	0.7
BCHII	$0.31^{+0.014}_{-0.013}$	$1.04^{+1.234}_{-0.729}$	$67.62^{+1.068}_{-1.130}$	$0.69^{+0.033}_{-0.032}$	$-0.91^{+0.074}_{-0.077}$	$-0.64^{+0.060}_{-0.059}$	408.18	1.7	414.18	424.62	1.95	5.43
SBCHII	$0.31^{+0.010}_{-0.010}$	$2.03^{+0.691}_{-0.661}$	$66.88^{+0.840}_{-0.847}$	$0.69^{+0.035}_{-0.034}$	$-0.85^{+0.039}_{-0.038}$	$-0.59^{+0.028}_{-0.027}$	2168.85	1.12	2174.85	2191.57	-9.4	-3.83
HS3												
SC	$0.33^{+0.026}_{-0.028}$	$5.02^{+1.001}_{-2.092}$	$66.84^{+1.684}_{-1.708}$	$0.70^{+0.115}_{-0.094}$	$-0.84^{+0.105}_{-0.071}$	$-0.56^{+0.057}_{-0.038}$	1772.23	1.02	1778.23	1794.6	-3.07	2.38
SBC	$0.31^{+0.011}_{-0.011}$	$5.62^{+0.643}_{-1.130}$	$66.54^{+1.030}_{-0.993}$	$0.76^{+0.040}_{-0.040}$	$-0.79^{+0.079}_{-0.064}$	$-0.54^{+0.055}_{-0.045}$	1798.35	1.02	1804.35	1820.77	-15.04	-9.57
SCHII	$0.31^{+0.026}_{-0.026}$	$5.24^{+0.673}_{-1.657}$	$68.53^{+1.216}_{-1.162}$	$0.78^{+0.113}_{-0.106}$	$-0.80^{+0.105}_{-0.083}$	$-0.56^{+0.062}_{-0.043}$	2137.24	1.12	2143.24	2159.9	-6.38	-0.83
BCHII	$0.31^{+0.013}_{-0.013}$	$2.96^{+1.657}_{-2.019}$	$67.93^{+1.824}_{-0.874}$	$0.72^{+0.038}_{-0.038}$	$-0.90^{+0.072}_{-0.072}$	$-0.62^{+0.057}_{-0.057}$	408.21	1.7	414.21	424.65	1.99	5.46
SBCHII	$0.32^{+0.010}_{-0.010}$	$5.01^{+0.924}_{-1.389}$	$67.42^{+0.827}_{-0.883}$	$0.73^{+0.036}_{-0.037}$	$-0.83^{+0.065}_{-0.052}$	$-0.57^{+0.046}_{-0.037}$	2166.71	1.12	2172.71	2189.42	-11.54	-5.97
EXP												
SC	$0.31^{+0.036}_{-0.042}$	$2.34^{+0.597}_{-0.792}$	$66.97^{+1.729}_{-1.738}$	$0.73^{+0.160}_{-0.126}$	$-0.83^{+0.093}_{-0.090}$	$-0.56^{+0.044}_{-0.041}$	1773.24	1.02	1779.24	1795.61	-2.07	3.39
SBC	$0.31^{+0.011}_{-0.011}$	$2.42^{+0.365}_{-0.390}$	$66.05^{+1.097}_{-1.102}$	$0.78^{+0.043}_{-0.042}$	$-0.79^{+0.050}_{-0.048}$	$-0.54^{+0.034}_{-0.033}$	1799.21	1.02	1805.21	1821.63	-14.18	-8.71
SCHII	$0.28^{+0.036}_{-0.041}$	$2.55^{+0.436}_{-0.659}$	$68.68^{+1.242}_{-1.185}$	$0.83^{+0.166}_{-0.137}$	$-0.79^{+0.086}_{-0.086}$	$-0.55^{+0.043}_{-0.041}$	2138.92	1.12	2144.92	2161.58	-4.7	0.85
BCHII	$0.30^{+0.014}_{-0.013}$	$1.16^{+0.940}_{-0.812}$	$68.21^{+0.869}_{-1.208}$	$0.72^{+0.048}_{-0.046}$	$-0.93^{+0.102}_{-0.068}$	$-0.65^{+0.080}_{-0.053}$	408.22	1.7	414.22	424.67	2.0	5.47
SBCHII	$0.32^{+0.010}_{-0.010}$	$2.10^{+0.372}_{-0.383}$	$67.21^{+0.899}_{-0.883}$	$0.76^{+0.037}_{-0.036}$	$-0.83^{+0.044}_{-0.044}$	$-0.56^{+0.031}_{-0.031}$	2167.67	1.12	2173.67	2190.38	-10.58	-5.01
TSUJI												
SC	$0.33^{+0.032}_{-0.036}$	$4.32^{+0.828}_{-1.398}$	$66.91^{+1.743}_{-1.704}$	$0.73^{+0.160}_{-0.126}$	$-0.83^{+0.093}_{-0.090}$	$-0.56^{+0.044}_{-0.041}$	1772.91	1.02	1778.91	1795.28	-2.39	3.06
SBC	$0.31^{+0.011}_{-0.011}$	$4.74^{+0.552}_{-0.649}$	$66.36^{+1.107}_{-1.067}$	$0.78^{+0.043}_{-0.042}$	$-0.79^{+0.050}_{-0.048}$	$-0.54^{+0.034}_{-0.033}$	1799.12	1.02	1805.12	1821.54	-14.27	-8.8
SCHII	$0.30^{+0.032}_{-0.035}$	$4.60^{+0.559}_{-1.019}$	$68.58^{+1.247}_{-1.196}$	$0.83^{+0.166}_{-0.137}$	$-0.79^{+0.086}_{-0.086}$	$-0.55^{+0.043}_{-0.041}$	2138.49	1.12	2144.49	2161.15	-5.13	0.42
BCHII	$0.31^{+0.015}_{-0.013}$	$2.35^{+1.877}_{-1.663}$	$68.33^{+0.829}_{-1.069}$	$0.72^{+0.048}_{-0.046}$	$-0.93^{+0.102}_{-0.068}$	$-0.65^{+0.080}_{-0.053}$	408.22	1.7	414.22	424.66	2.0	5.47
SBCHII	$0.32^{+0.010}_{-0.010}$	$4.29^{+0.590}_{-0.701}$	$67.39^{+0.886}_{-0.879}$	$0.76^{+0.037}_{-0.036}$	$-0.83^{+0.044}_{-0.044}$	$-0.56^{+0.031}_{-0.031}$	2167.17	1.12	2173.17	2189.88	-11.08	-5.51
aTanh												
SC	$0.27^{+0.041}_{-0.042}$	$1.69^{+0.865}_{-0.856}$	$67.08^{+1.659}_{-1.707}$	$0.79^{+0.186}_{-0.137}$	$-0.78^{+0.065}_{-0.077}$	$-0.57^{+0.027}_{-0.031}$	1773.73	1.03	1779.73	1796.1	-1.57	3.88
SBC	$0.30^{+0.012}_{-0.011}$	$0.99^{+0.412}_{-0.339}$	$65.02^{+1.158}_{-1.169}$	$0.68^{+0.036}_{-0.035}$	$-0.84^{+0.035}_{-0.039}$	$-0.59^{+0.026}_{-0.026}$	1800.58	1.02	1806.58	1823.0	-12.81	-7.34
SCHII	$0.25^{+0.036}_{-0.035}$	$1.87^{+0.721}_{-0.768}$	$68.65^{+1.188}_{-1.151}$	$0.88^{+0.177}_{-0.142}$	$-0.76^{+0.052}_{-0.065}$	$-0.58^{+0.025}_{-0.028}$	2139.45	1.12	2145.45	2162.12	-4.17	1.39
BCHII	$0.30^{+0.012}_{-0.011}$	$0.24^{+0.334}_{-0.169}$	$67.68^{+0.986}_{-1.190}$	$0.67^{+0.031}_{-0.033}$	$-0.95^{+0.065}_{-0.037}$	$-0.66^{+0.051}_{-0.031}$	408.2	1.7	414.2	424.64	1.97	5.45
SBCHII	$0.31^{+0.010}_{-0.010}$	$0.59^{+0.290}_{-0.225}$	$66.67^{+0.958}_{-0.938}$	$0.65^{+0.030}_{-0.029}$	$-0.88^{+0.036}_{-0.038}$	$-0.61^{+0.026}_{-0.027}$	2171.09	1.12	2177.09	2193.81	-7.16	-1.59

5. For all data sets (except SC), the values of Ω_{m0} are compatible with $\Omega_{m0,\text{Planck}}$ within 1-2(3) sigma. There is a tension of approximately 1.5-3 sigma between the values of H_0 when comparing the cases with and without the SH0ES prior for H_0 . There exists more or less same order of tensions between the fitted values of H_0 and $H_{0,\text{Planck}}$ or $H_{0,\text{SH0ES}}$.

B. Constraints on Hu-Sawicki Model and Starobinsky Model

Previous studies (see [18] and references therein) have established that there exists a degeneracy between $n_{\text{HS}}/n_{\text{s}}$ and Ω_{m0} . One, therefore, often works with fixed values of n_{HS} and n_{s} to address this degeneracy. In [83], it has been worked out that $n_{\text{HS}}, n_{\text{s}} > 0.9$, while

TABLE II. Results from the MCMC fitting process(for the cases with SH0ES prior for H_0): The median values of the model parameters along with 1-sigma(68.26%) confidence intervals on them, the transition redshift(z_t), the current values of EoS parameter for geometric/dark energy component(w_{DE0}) and total EoS parameter(w_{tot0}), the minimum values of χ^2 and other quantities for making statistical inferences such as the reduced chi-square value $\chi^2_{red} = \chi^2_{min}/\nu$ (where the number of degrees of freedom $\nu = N - k$, N is the total number of data points and k is the number of model parameters), the Akaike Information Criterion(AIC), the Bayesian Information Criterion(BIC), $\Delta AIC = AIC_{f(R) \text{ model}} - AIC_{\Lambda\text{CDM model}}$ and $\Delta BIC = BIC_{f(R) \text{ model}} - BIC_{\Lambda\text{CDM model}}$ for all the models and data set combinations considered in this work.

Data	Ω_{m0}	b	H_0	z_t	w_{DE0}	w_{tot0}	χ^2	χ^2_{red}	AIC	BIC	ΔAIC	ΔBIC
ACDM												
SCH_0	$0.34^{+0.016}_{-0.016}$	—	$71.28^{+0.898}_{-0.887}$	$0.58^{+0.038}_{-0.037}$	-1	$-0.66^{+0.016}_{-0.016}$	1788.16	1.03	1792.16	1803.07	0.0	0.0
$SBCH_0$	$0.32^{+0.010}_{-0.010}$	—	$70.40^{+0.591}_{-0.589}$	$0.61^{+0.025}_{-0.024}$	-1	$-0.68^{+0.010}_{-0.010}$	1824.91	1.04	1828.91	1839.86	0.0	0.0
$SCH_{II}H_0$	$0.33^{+0.015}_{-0.015}$	—	$70.98^{+0.799}_{-0.794}$	$0.60^{+0.038}_{-0.036}$	-1	$-0.67^{+0.015}_{-0.015}$	2154.83	1.13	2158.83	2169.94	0.0	0.0
$BCH_{II}H_0$	$0.30^{+0.011}_{-0.011}$	—	$69.97^{+0.547}_{-0.546}$	$0.66^{+0.028}_{-0.028}$	-1	$-0.70^{+0.011}_{-0.011}$	420.25	1.74	424.25	431.23	0.0	0.0
$SBCH_{II}H_0$	$0.32^{+0.010}_{-0.009}$	—	$70.25^{+0.552}_{-0.541}$	$0.62^{+0.023}_{-0.023}$	-1	$-0.68^{+0.010}_{-0.009}$	2190.08	1.13	2194.08	2205.23	0.0	0.0
HS1												
SCH_0	$0.24^{+0.036}_{-0.031}$	$1.55^{+0.499}_{-0.630}$	$71.43^{+0.897}_{-0.889}$	$0.89^{+0.168}_{-0.145}$	$-0.77^{+0.054}_{-0.067}$	$-0.59^{+0.027}_{-0.029}$	1782.1	1.03	1788.1	1804.47	-4.06	1.4
$SBCH_0$	$0.32^{+0.010}_{-0.010}$	$0.15^{+0.134}_{-0.101}$	$69.70^{+0.735}_{-0.799}$	$0.61^{+0.022}_{-0.025}$	$-0.97^{+0.032}_{-0.019}$	$-0.66^{+0.026}_{-0.016}$	1824.39	1.04	1830.39	1846.81	1.48	6.95
$SCH_{II}H_0$	$0.23^{+0.033}_{-0.027}$	$1.67^{+0.432}_{-0.581}$	$71.18^{+0.780}_{-0.823}$	$0.96^{+0.158}_{-0.149}$	$-0.76^{+0.048}_{-0.061}$	$-0.59^{+0.026}_{-0.029}$	2146.44	1.12	2152.44	2169.1	-6.39	-0.84
$BCH_{II}H_0$	$0.31^{+0.011}_{-0.011}$	$0.05^{+0.068}_{-0.035}$	$69.76^{+0.578}_{-0.575}$	$0.65^{+0.029}_{-0.028}$	$-0.99^{+0.011}_{-0.005}$	$-0.69^{+0.014}_{-0.013}$	420.28	1.74	426.28	436.73	2.03	5.51
$SBCH_{II}H_0$	$0.32^{+0.010}_{-0.010}$	$0.14^{+0.121}_{-0.091}$	$69.69^{+0.642}_{-0.688}$	$0.62^{+0.025}_{-0.024}$	$-0.98^{+0.028}_{-0.016}$	$-0.66^{+0.020}_{-0.015}$	2189.75	1.13	2195.75	2212.46	1.67	7.24
ST1/HS2												
SCH_0	$0.27^{+0.029}_{-0.032}$	$2.85^{+0.601}_{-0.971}$	$71.45^{+0.901}_{-0.873}$	$0.86^{+0.168}_{-0.132}$	$-0.79^{+0.084}_{-0.069}$	$-0.57^{+0.044}_{-0.035}$	1781.71	1.03	1787.71	1804.08	-4.45	1.01
$SBCH_0$	$0.32^{+0.010}_{-0.010}$	$0.83^{+0.578}_{-0.445}$	$69.51^{+0.800}_{-0.799}$	$0.63^{+0.030}_{-0.029}$	$-0.94^{+0.045}_{-0.050}$	$-0.63^{+0.033}_{-0.034}$	1823.2	1.04	1829.2	1845.62	0.28	5.75
$SCH_{II}H_0$	$0.26^{+0.030}_{-0.031}$	$3.03^{+0.440}_{-0.889}$	$71.19^{+0.802}_{-0.820}$	$0.94^{+0.179}_{-0.144}$	$-0.77^{+0.084}_{-0.074}$	$-0.57^{+0.047}_{-0.038}$	2145.93	1.12	2151.93	2168.6	-6.89	-1.34
$BCH_{II}H_0$	$0.31^{+0.011}_{-0.011}$	$0.21^{+0.238}_{-0.147}$	$69.85^{+0.577}_{-0.579}$	$0.66^{+0.028}_{-0.028}$	$-1.00^{+0.015}_{-0.003}$	$-0.69^{+0.016}_{-0.012}$	420.25	1.74	426.25	436.71	2.0	5.48
$SBCH_{II}H_0$	$0.32^{+0.010}_{-0.009}$	$0.75^{+0.521}_{-0.427}$	$69.53^{+0.727}_{-0.723}$	$0.64^{+0.027}_{-0.027}$	$-0.94^{+0.046}_{-0.046}$	$-0.64^{+0.033}_{-0.031}$	2188.66	1.13	2194.66	2211.38	0.58	6.15
HS3												
SCH_0	$0.30^{+0.025}_{-0.026}$	$4.98^{+0.715}_{-1.683}$	$71.42^{+0.901}_{-0.885}$	$0.80^{+0.114}_{-0.107}$	$-0.82^{+0.100}_{-0.077}$	$-0.57^{+0.057}_{-0.041}$	1780.99	1.03	1786.99	1803.36	-5.17	0.29
$SBCH_0$	$0.33^{+0.010}_{-0.010}$	$3.38^{+1.213}_{-1.363}$	$69.55^{+0.678}_{-0.671}$	$0.67^{+0.033}_{-0.033}$	$-0.90^{+0.035}_{-0.030}$	$-0.60^{+0.026}_{-0.024}$	1820.05	1.03	1826.05	1842.47	-2.87	2.61
$SCH_{II}H_0$	$0.28^{+0.024}_{-0.024}$	$5.12^{+0.539}_{-1.393}$	$71.14^{+0.817}_{-0.773}$	$0.85^{+0.108}_{-0.108}$	$-0.79^{+0.097}_{-0.089}$	$-0.56^{+0.059}_{-0.045}$	2144.92	1.12	2150.92	2167.59	-7.91	-2.35
$BCH_{II}H_0$	$0.31^{+0.011}_{-0.012}$	$0.57^{+0.402}_{-0.402}$	$69.78^{+0.579}_{-0.579}$	$0.67^{+0.029}_{-0.029}$	$-0.99^{+0.006}_{-0.006}$	$-0.68^{+0.016}_{-0.016}$	420.23	1.74	426.23	436.68	1.98	5.45
$SBCH_{II}H_0$	$0.32^{+0.010}_{-0.010}$	$3.23^{+1.198}_{-1.289}$	$69.49^{+0.594}_{-0.622}$	$0.68^{+0.032}_{-0.032}$	$-0.90^{+0.034}_{-0.029}$	$-0.61^{+0.025}_{-0.023}$	2185.47	1.13	2191.47	2208.19	-2.61	2.96
EXP												
SCH_0	$0.27^{+0.036}_{-0.040}$	$2.48^{+0.473}_{-0.662}$	$71.46^{+0.888}_{-0.891}$	$0.85^{+0.172}_{-0.140}$	$-0.80^{+0.085}_{-0.084}$	$-0.56^{+0.042}_{-0.040}$	1781.83	1.03	1787.83	1804.2	-4.32	1.13
$SBCH_0$	$0.33^{+0.010}_{-0.010}$	$1.41^{+0.381}_{-0.466}$	$69.75^{+0.732}_{-0.758}$	$0.68^{+0.034}_{-0.038}$	$-0.90^{+0.039}_{-0.042}$	$-0.61^{+0.030}_{-0.031}$	1820.84	1.03	1826.84	1843.26	-2.08	3.4
$SCH_{II}H_0$	$0.26^{+0.036}_{-0.038}$	$2.62^{+0.392}_{-0.873}$	$71.22^{+0.807}_{-0.801}$	$0.93^{+0.189}_{-0.147}$	$-0.77^{+0.084}_{-0.084}$	$-0.56^{+0.043}_{-0.041}$	2146.11	1.12	2152.11	2168.78	-6.71	-1.16
$BCH_{II}H_0$	$0.31^{+0.011}_{-0.011}$	$0.47^{+0.412}_{-0.318}$	$69.92^{+0.562}_{-0.571}$	$0.67^{+0.033}_{-0.032}$	$-1.00^{+0.050}_{-0.005}$	$-0.68^{+0.036}_{-0.017}$	420.24	1.74	426.24	436.7	2.0	5.47
$SBCH_{II}H_0$	$0.32^{+0.010}_{-0.010}$	$1.36^{+0.368}_{-0.449}$	$69.68^{+0.658}_{-0.662}$	$0.69^{+0.033}_{-0.036}$	$-0.90^{+0.038}_{-0.041}$	$-0.61^{+0.029}_{-0.030}$	2185.98	1.13	2191.98	2208.69	-2.1	3.47
TSUJI												
SCH_0	$0.29^{+0.032}_{-0.035}$	$4.44^{+0.569}_{-1.031}$	$71.45^{+0.892}_{-0.896}$	$0.85^{+0.172}_{-0.140}$	$-0.80^{+0.085}_{-0.084}$	$-0.56^{+0.042}_{-0.040}$	1781.6	1.03	1787.6	1803.97	-4.56	0.89
$SBCH_0$	$0.33^{+0.010}_{-0.010}$	$3.13^{+0.740}_{-0.873}$	$69.82^{+0.717}_{-0.723}$	$0.68^{+0.034}_{-0.038}$	$-0.90^{+0.039}_{-0.042}$	$-0.61^{+0.030}_{-0.031}$	1819.49	1.03	1825.49	1841.91	-3.43	2.04
$SCH_{II}H_0$	$0.27^{+0.032}_{-0.034}$	$4.58^{+0.447}_{-0.856}$	$71.19^{+0.787}_{-0.811}$	$0.93^{+0.189}_{-0.147}$	$-0.77^{+0.084}_{-0.084}$	$-0.56^{+0.043}_{-0.041}$	2145.82	1.12	2151.82	2168.49	-7.0	-1.45
$BCH_{II}H_0$	$0.31^{+0.012}_{-0.011}$	$1.06^{+1.069}_{-0.731}$	$69.91^{+0.559}_{-0.570}$	$0.67^{+0.033}_{-0.032}$	$-1.00^{+0.050}_{-0.005}$	$-0.68^{+0.036}_{-0.017}$	420.22	1.74	426.22	436.67	1.97	5.44
$SBCH_{II}H_0$	$0.32^{+0.010}_{-0.010}$	$3.05^{+0.713}_{-0.847}$	$69.73^{+0.658}_{-0.649}$	$0.69^{+0.033}_{-0.036}$	$-0.90^{+0.038}_{-0.041}$	$-0.61^{+0.029}_{-0.030}$	2184.7	1.12	2190.7	2207.41	-3.38	2.19
aTanh												
SCH_0	$0.24^{+0.035}_{-0.030}$	$1.75^{+0.627}_{-0.752}$	$71.47^{+0.868}_{-0.879}$	$0.90^{+0.155}_{-0.140}$	$-0.77^{+0.047}_{-0.066}$	$-0.59^{+0.024}_{-0.027}$	1782.11	1.03	1788.11	1804.48	-4.05	1.41
$SBCH_0$	$0.32^{+0.010}_{-0.010}$	$0.16^{+0.139}_{-0.104}$	$69.65^{+0.764}_{-0.781}$	$0.61^{+0.026}_{-0.026}$	$-0.97^{+0.034}_{-0.022}$	$-0.65^{+0.023}_{-0.018}$	1824.32	1.04	1830.32	1846.74	1.4	6.88
$SCH_{II}H_0$	$0.23^{+0.033}_{-0.027}$	$1.86^{+0.555}_{-0.705}$	$71.17^{+0.770}_{-0.770}$	$0.96^{+0.151}_{-0.144}$	$-0.76^{+0.041}_{-0.059}$	$-0.59^{+0.023}_{-0.026}$	2146.48	1.12	2152.48	2169.15	-6.34	-0.79
$BCH_{II}H_0$	$0.31^{+0.011}_{-0.011}$	$0.05^{+0.066}_{-0.034}$	$69.76^{+0.579}_{-0.587}$	$0.66^{+0.029}_{-0.029}$	$-0.99^{+0.012}_{-0.006}$	$-0.69^{+0.015}_{-0.013}$	420.27	1.74	426.27	436.73	2.02	5.5
$SBCH_{II}H_0$	$0.32^{+0.010}_{-0.009}$	$0.14^{+0.128}_{-0.092}$	$69.64^{+0.677}_{-0.690}$	$0.62^{+0.024}_{-0.024}$	$-0.97^{+0.031}_{-0.019}$	$-0.66^{+0.022}_{-0.016}$	2189.68	1.13	2195.68	2212.4	1.6	7.17

[84] proposed that n_{HS} and n_S should be integers. The difficulty in constraining higher n_{HS}/n_S values due to numerical instability issues while solving the modified Hubble equations is also well known. Consequently, it has become common practice to work with $n_{HS} = 1$ and $n_S = 1$. In our study we have also explored the case of $n_{HS} = 3$. Note that in the re-parameterized version using the deviation parameter b , the Hu-Sawicki model

with $n_{HS} = 2$ is equivalent to the Starobinsky model with $n_S = 1$.

The quantitative results of fitting the Hu-Sawicki model (Eq. 27) with $n_{HS} = 1, 3$ and the Starobinsky model (Eq. 29) with $n_S = 1$, following the procedure discussed in Sec. IV, are presented in the Tables I and II. The 2D contour plots of the posterior probability dis-

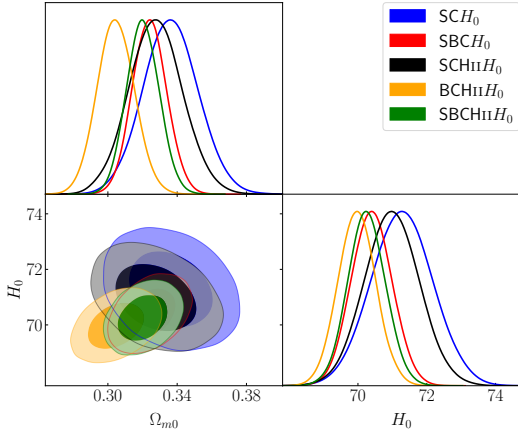


FIG. 5. The Λ CDM Model (with SH0ES prior for H_0): The posterior probability distribution plots of fitted parameters. The color correspondence for different data-set combinations can be seen in the figure legends. The darker and lighter shades of colors represent 1-sigma (68.26%) and 2-sigma (95.44%) confidence intervals, respectively.

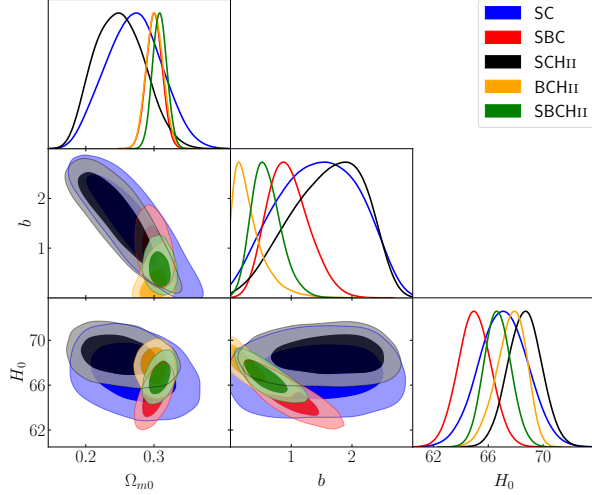


FIG. 6. The Hu-Sawicki Model ($n_{\text{HS}} = 1$, without SH0ES prior for H_0): The posterior probability distribution plots of fitted parameters. The color correspondence for different data-set combinations can be seen in the figure legends. The darker and lighter shades of colors represent 1-sigma (68.26%) and 2-sigma (95.44%) confidence intervals, respectively.

tribution of the model parameters and 1D marginalised distribution of each of the parameters are shown in the Figs. 6 and 7 (for $n_{\text{HS}} = 1$), Figs. 8 and 9 (for $n_{\text{HS}} = 2$ or, $n_{\text{S}} = 1$), Figs. 10 and 11 (for $n_{\text{HS}} = 3$), for the respective cases - without and with the SH0ES prior for H_0 .

The Fig. 1 illustrates that as n_{HS} increases (from 1 to 3) the values of Ω_{m0} approach closer to those from the Λ CDM model (and/or to $\Omega_{m0, \text{Planck}}$) and the constraints on them become tighter. This applies to both cases with and without the SH0ES prior for H_0 . We may observe

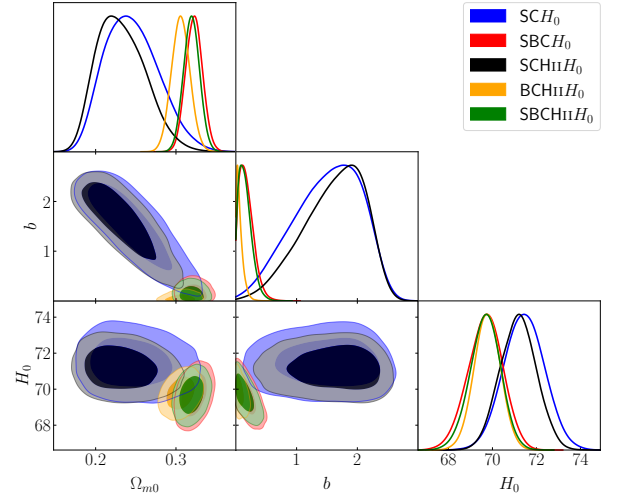


FIG. 7. The Hu-Sawicki Model ($n_{\text{HS}} = 1$, with SH0ES prior for H_0): The posterior probability distribution plots of fitted parameters. The color correspondence for different data-set combinations can be seen in the figure legends. The darker and lighter shades of colors represent 1-sigma (68.26%) and 2-sigma (95.44%) confidence intervals, respectively.

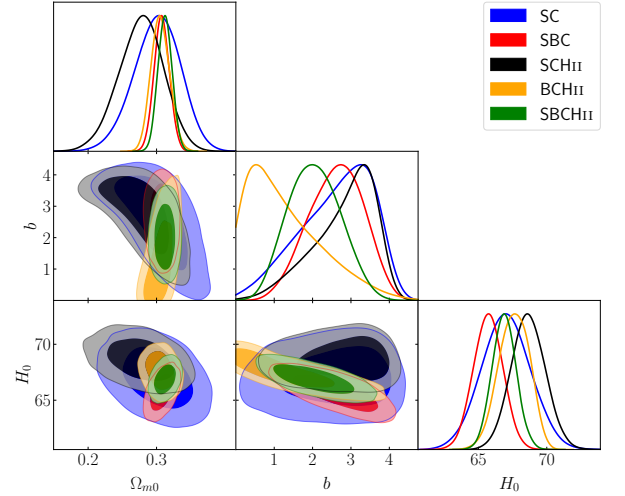


FIG. 8. The Starobinsky Model ($n_{\text{S}} = 1$, without SH0ES prior for H_0): The posterior probability distribution plots of fitted parameters. The color correspondence for different data-set combinations can be seen in the figure legends. The darker and lighter shades of colors represent 1-sigma (68.26%) and 2-sigma (95.44%) confidence intervals, respectively.

from Fig. 3 that when the SH0ES prior for H_0 is not considered, increasing n_{HS} causes the model values of H_0 to approach $H_{0, \text{Planck}}$, except for the SC dataset where there is almost no change with varying n_{HS} . However, the constraints from the BCHII dataset are not considered reliable due to high χ^2/ν . When the SH0ES prior is included, there is hardly any change in the model values of H_0 with respect to n_{HS} , and they lie around $69.5 - 71.5 \text{ km s}^{-1} \text{ Mpc}^{-1}$. As expected, the parameter b increases as

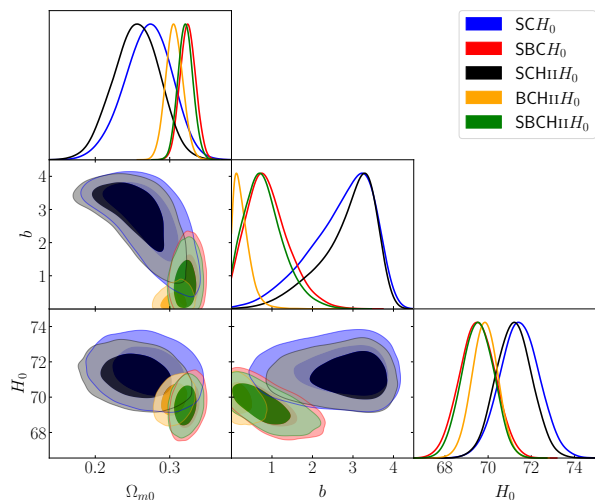


FIG. 9. The Starobinsky Model($n_s = 1$, with SH0ES prior for H_0): The posterior probability distribution plots of fitted parameters. The color correspondence for different data-set combinations can be seen in the figure legends. The darker and lighter shades of colors represent 1-sigma(68.26%) and 2-sigma(95.44%) confidence intervals, respectively.

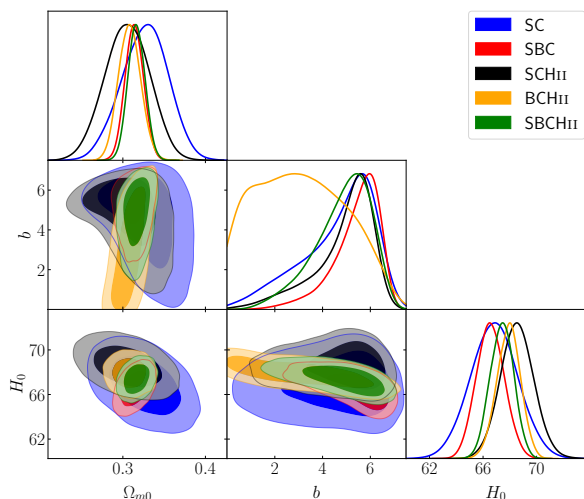


FIG. 10. The Hu-Sawicki Model($n_{\text{HS}} = 3$, without SH0ES prior for H_0): The posterior probability distribution plots of fitted parameters. The color correspondence for different data-set combinations can be seen in the figure legends. The darker and lighter shades of colors represent 1-sigma(68.26%) and 2-sigma(95.44%) confidence intervals, respectively.

n_{HS} increases (see Fig. 2). Also, the constraints on b become weaker. We may infer that for higher values of n_{HS} (say 4, 5, ...) and n_s (say 2, 3, ..), the constraints on b would become even more weaker. This implies that with further increase in n_{HS} or n_s , one can obtain a model that closely resembles the Λ CDM model in terms of its predictions for the physical parameters Ω_{m0} and H_0 , despite the constraints on b moving towards larger values. In a sense, this undermines the purpose of explor-

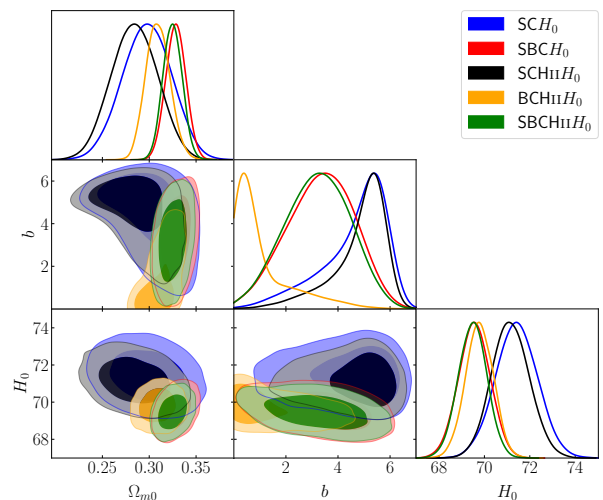


FIG. 11. The Hu-Sawicki Model($n_{\text{HS}} = 3$, with SH0ES prior for H_0): The posterior probability distribution plots of fitted parameters. The color correspondence for different data-set combinations can be seen in the figure legends. The darker and lighter shades of colors represent 1-sigma(68.26%) and 2-sigma(95.44%) confidence intervals, respectively.

ing $f(R)$ models further, and there is a strategic motivation to limit the exploration to $n_{\text{HS}} = 1, 2$ only, putting aside the consideration of computational difficulties in constraining for the higher values of n_{HS} or n_s . For all three models, there are instances where $b = 0$ is only very marginally allowed (i.e., within a 2-3 sigma limit), indicating distinguishable models from the Λ CDM model. This finding is also an important result of the present work.

C. Constraints on Exponential Model

In the Tables I and II, we present the median values and 1-sigma (68.26%) confidence intervals for the parameters of the exponential model (Eq. 31). The corresponding 2D contour plots illustrating the posterior probability distribution of the parameters, along with the 1D marginal distributions for each parameter, are depicted in Figs 12 and 13 for the cases - without and with the SH0ES prior for H_0 , respectively. We observe from Figs 12, 13, and 2 that except for the BCH II (H_0) dataset, the parameter b clearly deviates from zero, with $b = 0$ barely allowed. Despite this, the values of the parameters Ω_{m0} and H_0 (as illustrated in Figs. 1 and 3) are reasonably close to the standard values derived from Planck constraints [78]. The significance of this result becomes further clear in the subsequent section on model comparisons. When considering the SH0ES prior for H_0 , the range of model values of H_0 is ~ 69.7 to $71.5 \text{ km s}^{-1} \text{ Mpc}^{-1}$.

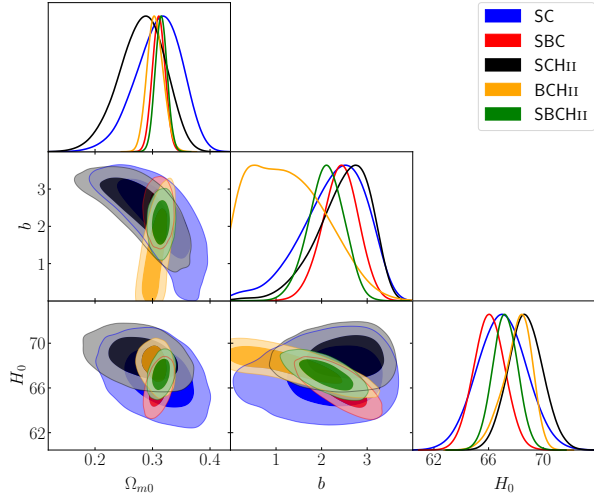


FIG. 12. The Exponential Model(without SH0ES prior for H_0): The posterior probability distribution plots of fitted parameters. The color correspondence for different data-set combinations can be seen in the figure legends. The darker and lighter shades of colors represent 1-sigma(68.26%) and 2-sigma(95.44%) confidence intervals, respectively.

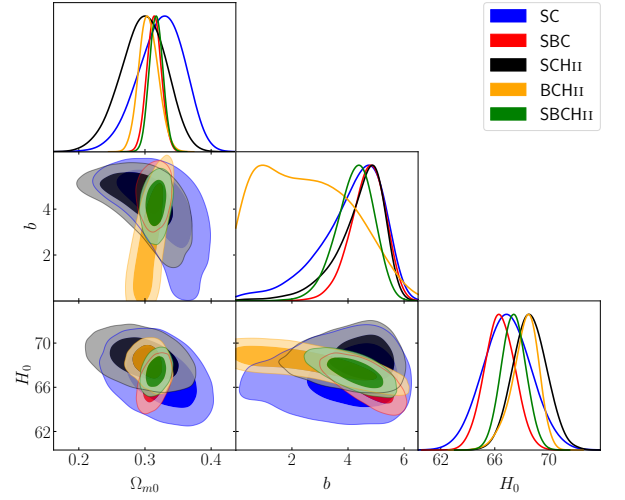


FIG. 14. The Tsujikawa Model(without SH0ES prior for H_0): The posterior probability distribution plots of fitted parameters. The color correspondence for different data-set combinations can be seen in the figure legends. The darker and lighter shades of colors represent 1-sigma(68.26%) and 2-sigma(95.44%) confidence intervals, respectively.

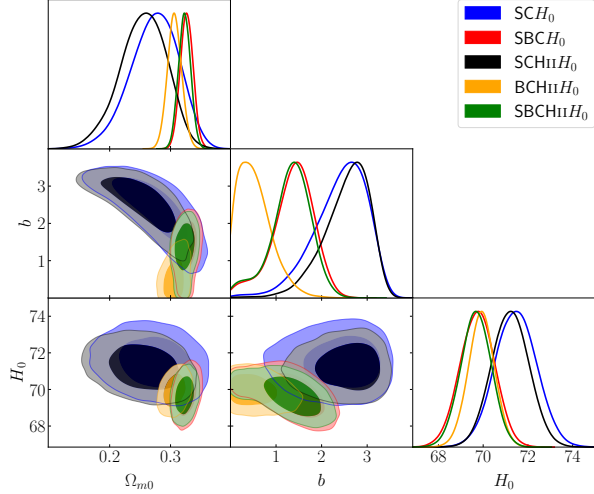


FIG. 13. The Exponential Model(with SH0ES prior for H_0): The posterior probability distribution plots of fitted parameters. The color correspondence for different data-set combinations can be seen in the figure legends. The darker and lighter shades of colors represent 1-sigma(68.26%) and 2-sigma(95.44%) confidence intervals, respectively.

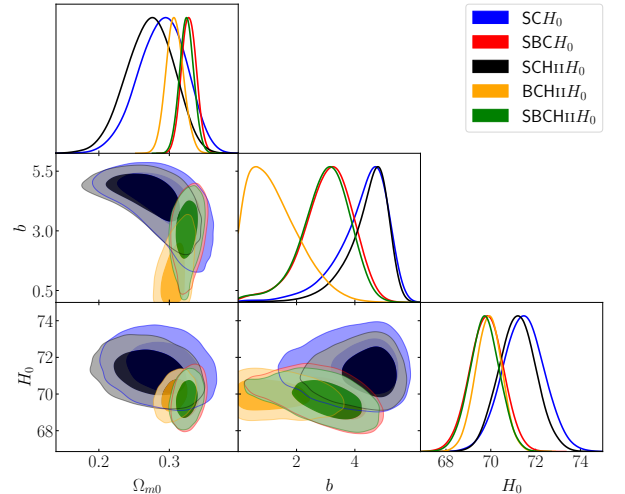


FIG. 15. The Tsujikawa Model(with SH0ES prior for H_0): The posterior probability distribution plots of fitted parameters. The color correspondence for different data-set combinations can be seen in the figure legends. The darker and lighter shades of colors represent 1-sigma(68.26%) and 2-sigma(95.44%) confidence intervals, respectively.

D. Constraints on Tsujikawa Model

The constraints on the parameters of the Tsujikawa model described by Eq. 33 are presented in the Tables I and II, as well as in Figs. 14 and 15. These constraints are shown separately for cases without and with the SH0ES prior on H_0 . Similar to the findings of the exponential model, here also we observe that the deviation parameter b is mostly nonzero, with only a very marginal

allowance for it to be zero, across all the datasets, except $BCHII(H_0)$. We disregard the results from $BCHII(H_0)$ on account of very high value of the reduced χ^2_{\min}/ν . Hence, we obtain an $f(R)$ that is clearly distinguishable from the Λ CDM model. The fitted values of Ω_{m0} and H_0 also fall within reasonable limits compared to $\Omega_{m0, \text{Planck}}$ and $H_{0, \text{Planck}}$ (or $H_{0, \text{SH0ES}}$). With SH0ES prior for H_0 , the model's median values for H_0 range from approximately 69.7 to 71.5 $\text{km s}^{-1}\text{Mpc}^{-1}$, which introduces a tension of

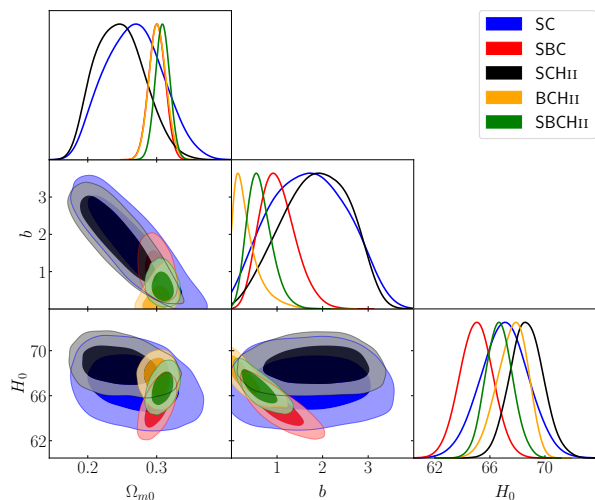


FIG. 16. The arcTanh Model(without SH0ES prior for H_0): The posterior probability distribution plots of fitted parameters. The color correspondence for different data-set combinations can be seen in the figure legends. The darker and lighter shades of colors represent 1-sigma(68.26%) and 2-sigma(95.44%) confidence intervals, respectively.

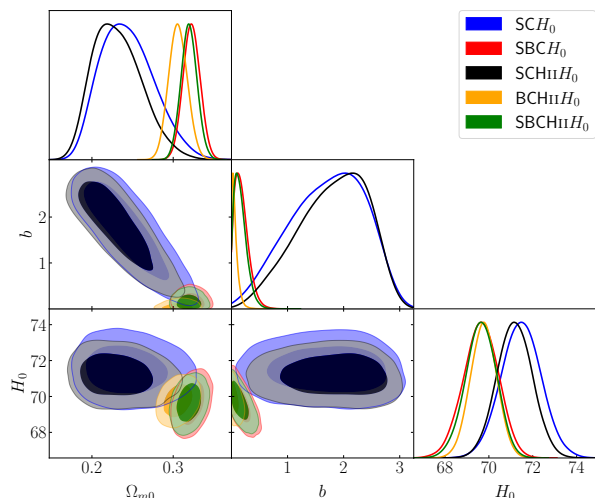


FIG. 17. The arcTanh Model(with SH0ES prior for H_0): The posterior probability distribution plots of fitted parameters. The color correspondence for different data-set combinations can be seen in the figure legends. The darker and lighter shades of colors represent 1-sigma(68.26%) and 2-sigma(95.44%) confidence intervals, respectively.

2-3 sigma with $H_{0,\text{Planck}}$ or $H_{0,\text{SH0ES}}$.

E. Constraints on arcTanh Model

The results obtained by constraining the aTanh model are presented in the Tables I and II, as well as in the Figs. 16 and 17, separately for cases without and with the SH0ES prior for H_0 . In several cases, excluding

BCHII(H_0), the parameter $b = 0$ falls well within the 1-2 sigma range. However, there are instances where $b = 0$ lies outside the 2-sigma range. In the subsequent section on model comparison, we will observe that these latter cases are also more favored, making this outcome significant. The fitted values of Ω_{m0} for the model fall within the 1-2 sigma range of $\Omega_{m0,\text{Planck}}$. Furthermore, $H_{0,\text{Planck}}$ is approximately within the 1-2 sigma range of that predicted by the model when the SH0ES prior is not considered. Upon inclusion of the SH0ES prior for H_0 , the model's predicted median values for H_0 range from approximately 69.65 to $71.47 \text{ km s}^{-1} \text{ Mpc}^{-1}$, which are in 2-3 sigma tension with $H_{0,\text{Planck}}$ or $H_{0,\text{SH0ES}}$.

It is important to highlight that the outcomes of this model are not significantly different from those of the HS1 model. This similarity would not sound surprising, if we examine Eqs 27 and 34 along with the fact that $\text{arctanh}(\Lambda/R) \approx \Lambda/R$ for $\Lambda/R \ll 1$ (which holds true in this case since $\Lambda \sim 0.7H_0^2$ and $R \gtrsim 8H_0^2$).

VI. MODEL COMPARISON

The standard statistical tools commonly used to assess model fitting (and model comparison) in cosmology include the reduced chi-square statistics (χ_ν^2), the Akaike Information Criterion (AIC) [85], and the Bayesian Information Criterion (BIC) [86] (also see [87–89]). The last six columns of Tables I and II contain essential quantities related to the current analysis, specifically pertaining to the utilization of these statistical tools. The reduced chi-square statistics is defined as $\chi_\nu^2 = \chi_{\text{min}}^2/\nu$ whereas the AIC and the BIC are respectively defined by the following equations

$$\text{AIC} = -2 \ln \mathcal{L}_{\text{max}} + 2k, \quad (54)$$

$$\text{BIC} = -2 \ln \mathcal{L}_{\text{max}} + k \ln N. \quad (55)$$

The number of degrees of freedom, represented by the symbol ν , is determined by subtracting the number of model parameters (k) from the total number of data points (N). The minimum value of χ^2 is denoted as χ_{min}^2 and is connected to the maximum likelihood (\mathcal{L}_{max}) through the relation $\chi_{\text{min}}^2 = -2 \ln \mathcal{L}_{\text{max}}$. While comparing multiple competing models using a given data set, the model with the lowest values of χ^2 , AIC, and BIC is considered to be more favoured by the data. However, it is insufficient to rely solely on χ^2 due to the principle of Occam's razor, which emphasizes the importance of considering the number of model parameters. Typically, for a nested model, as the number of parameters increases, the fit improves, leading to a decrease in χ_{min}^2 (or an increase in likelihood), regardless of the relevance of the newly included parameter(s). Both AIC and BIC incorporate a penalty term ($2k$ and $k \ln N$, respectively) that penalizes models with more parameters, in addition to the χ_{min}^2 term, taking into account any improvement

in fit. Thus a balance between the quality of fit and the complexity of the model is achieved through AIC and BIC. Comparing the Eqs. 54 and 55 for AIC and BIC, respectively, it can be observed that the penalty for models with a greater number of parameters is more severe in BIC than in AIC. Unfortunately, the conclusions derived from applying these two criteria may sometimes disagree. In such situations of disagreement, it is necessary to investigate whether any violations of the assumptions on which AIC and BIC are based have occurred (for details see [87–89]).

To perform a comparative analysis of two models, a useful measure $\Delta X = X_2 - X_1$, computed as the difference between the values of X ($=$ AIC or BIC) for the two models: 1 and 2, facilitates a quantitative assessment of the evidence supporting the preference of model 1 over model 2. A rule of thumb which is commonly followed as a guideline to indicate the degree of strength of the evidence with which the model 2 (model 1) is favoured over the other, is as follows: (i) $0 < \Delta X \leq 2$ ($-2 \leq \Delta X < 0$): weak evidence, (ii) $2 < \Delta X \leq 6$ ($-6 \leq \Delta X < -2$): positive evidence, (iii) $6 < \Delta X \leq 10$ ($-10 \leq \Delta X < -6$): strong evidence, (iv) $\Delta X > 10$ ($\Delta X < -10$): very strong (highly pronounced) evidence.

As can be seen from Tables I and II, the reduced χ^2 values for the BCHII(H_0) data-set do not come close to the value 1, for all the models. Consequently, these cases are not considered in our subsequent discussions related to model comparisons. The purpose of inclusion of these cases here is to illustrate that not all possible combinations of data-sets yield significantly meaningful results.

When we analyze different data-sets without considering the SH0ES prior for H_0 , we observe interesting patterns in Table I. The Δ AICs values indicate varying degrees of evidence ranging from weak to very strong in favor of $f(R)$ models compared to the Λ CDM model. On the other hand, the values of Δ BIC suggest evidence that is either weak or positive against $f(R)$ models in certain cases, while in other cases, the evidence is weak, positive, or even strong in favour of $f(R)$ models. The strongest support for all $f(R)$ models is from the SBC data-set, followed by the SBCHII data-set. In both cases, the trends of Δ AICs and Δ BICs align, guiding us in the same direction.

When the SH0ES prior for H_0 is included, the results, as shown in Table II, exhibit some differences. The overall support for $f(R)$ models weakens compared to the previous case. Based on consideration of the Δ AICs, the maximum support for any $f(R)$ model is now only strong (no longer very strong), and weak evidence against the $f(R)$ models is observed in a few cases. On the other hand, analyzing the Δ BICs for data-sets with the SH0ES prior for H_0 reveals weak, positive, or strong evidence against the $f(R)$ models when

compared to the Λ CDM model. Among the data-sets with the SH0ES prior for H_0 , the strongest evidence against the $f(R)$ models is observed in the SBCHII H_0 data-set, followed by the SBC H_0 data-set. Furthermore, Table II highlights that when a SH0ES prior for H_0 is employed, the evidence against models such as HS3, EXP, and TSUJI (which are more similar to the Λ CDM model) is weak or mildly positive according to Δ BIC. Conversely, for models such as HS1, aTanh, and ST (which are less or least similar to the Λ CDM model), the evidence against them is strong when evaluated using Δ BIC. Consequently, we can conclude that with a SH0ES prior for H_0 , the Δ BIC criterion disfavors models that significantly deviate from the Λ CDM model.

A crucial observation to note is that the cases of $f(R)$ models with strong or very strong evidence for being preferred over the Λ CDM model (as indicated by Δ AIC and/or Δ BIC) also correspond to the cases where a non-zero value of the deviation parameter b is favored, with the possibility of a very marginal acceptance of $b = 0$. This finding is an important result of this study, which can be observed from Figs. 6-17 and Tables I and II.

VII. ACCELERATED EXPANSION OF THE UNIVERSE

In this section we discuss the findings regarding the relevant quantities that describe the current accelerated expansion of the universe. The behavior of the deceleration parameter ($q(z)$), which is defined as $q(z) \equiv -\ddot{a}/\dot{a}^2 = -\ddot{a}/(H^2 a)$, provides valuable insight into whether the cosmic expansion is accelerating ($q < 0$) or decelerating ($q > 0$), serving as an indicator of the respective phases. Through several model-independent measurements of $q(z)$, it has been observed that $q(z = 0) < 0$ and $q(z > z_t) > 0$ [90, 91]. The quantity z_t , called transition redshift, indicates the redshift at which the universe has undergone transition from a decelerated phase to an accelerated phase of expansion.

The total equation-of-state (EoS) parameter (w_{eff}) as a function of redshift provides valuable information about the evolution of the universe through the eras of radiation domination, matter domination, and the subsequent late time accelerated phase of expansion dubbed as dark energy era. During these three phases, w_{eff} takes values approximately equal to 1/3, 0, and -1 (for Λ CDM). On the other hand, the EoS parameter (w_{DE}) associated with the dark energy component remains constant at -1 for all values of redshift (both in the past and future) in Λ CDM model. However, in the case of any viable $f(R)$ model, value of the parameter w_{DE} can cross the so called ‘‘phantom-divide’’ line ($w_{\text{DE}}(z) = -1$) multiple times before finally settling at -1 in the far future [92, 93].

In the Tables I and II we present the median values

and 1-sigma confidence intervals for the quantities z_t , $w_{\text{DE},0}$, and $w_{\text{eff},0}$ for two cases - without and with the SH0ES prior on H_0 . In Fig 18, we display the values of z_t for all models and data-sets. This figure shows the median values of $z_t \sim 0.5 - 1$ for all the models, which is compatible with the model-independent predictions for z_t [90, 91]. In the Figs. 19 and 20 we have plotted the evolution of w_{DE} with redshift based on the best constraints obtained for the models, (which happens to be the constraints from the data-set SCHII(H_0)). In all $f(R)$ models, the values of $w_{\text{DE}}(z)$ mark a crossover from the so-called “phantom regime” in the distant past to the so-called “quintessence regime” in the more recent past, with the present-epoch values ($w_{\text{DE},0}$) falling within the quintessence region. When the SH0ES prior on H_0 is included, the deviations of $w_{\text{DE}}(z)$ for $f(R)$ models from the Λ CDM model are reduced and the transition from the phantom regime to the quintessence regime happens more recently compared to the situation without the SH0ES prior.

For any viable $f(R)$ model, the $w_{\text{DE}}(z)$ curve is expected to eventually reach a stable, constant value of -1 in the distant past - a behavior which is necessary to account for the matter-dominated era in the context of the model. From Figs. 19 and 20, we can readily observe that the Tsujikawa model and the Exponential model exhibit a clear convergence to -1 , while for the other models this convergence takes place in a more remote past, characterized by higher values of z . The trend for possible future crossing into phantom regime is clearly visible for the HS1 model, the Starobinsky model and the aTanh model, whereas this trend is not as apparent in the other models. However, theoretical studies [92, 93] have indicated that these models are also expected to cross the phantom divide in the future, albeit in an oscillatory manner. Although it would be an intriguing future project to extend the analysis of the $w_{\text{DE}}(z)$ curve up to $z \rightarrow -1 (a \rightarrow \infty)$, it is beyond the scope of the present work. This is due to the potential limitations of the employed ODE system, which may not accurately capture the oscillatory features in such a far future regime.

The behavior of $w_{\text{eff}}(z)$ is depicted in Figs. 21 and 22, revealing a transition from a matter-dominated era (represented by $w_{\text{eff}}(z) \rightarrow 0$) to a dark energy dominated era around $z \sim 5$ for all the $f(R)$ models. Considering the SH0ES prior for H_0 leads to relatively lower values of $w_{\text{eff},0}$ for all the $f(R)$ models compared to the cases without the prior. Furthermore, the discrepancy between the predictions of $w_{\text{eff}}(z)$ obtained from the Λ CDM model and those from the $f(R)$ models reduces when the SH0ES prior is included.

VIII. CONCLUSIONS

In this study, we used the recently released Pantheon-plus SNIa data along with cosmic chronometer measure-

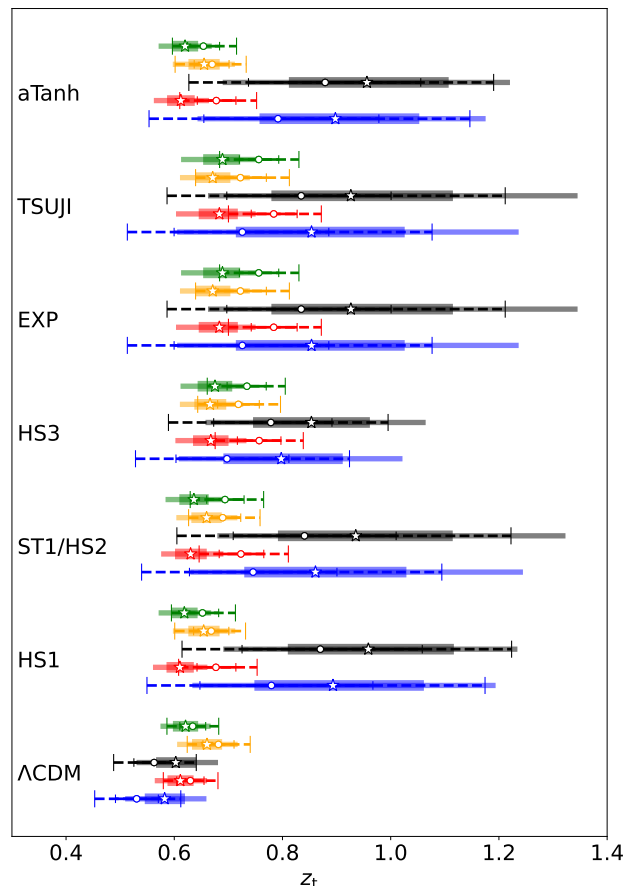


FIG. 18. Transition Redshift: The blank star and blank circle markers represent median values for the cases with and without SH0ES prior for H_0 , respectively. Different colors represent different data-set combinations and these are same as in any of the parameter distribution plots (e.g. Fig. 6) or see 2nd paragraph of Sec.V. The thick and thin horizontal colored bars represent 1-sigma(68.26%) and 2-sigma(95.44%) confidence intervals for the cases with SH0ES prior. The colored continuous/dashed lines represent 1-sigma(68.26%, with smaller cap size) and 2-sigma(95.44%, with bigger cap size) confidence intervals for the cases without SH0ES prior.

ments, baryonic acoustic oscillation measurements, HII starburst galaxies data, and the local measurement of the Hubble parameter, to constrain popularly studied $f(R)$ models in the metric formalism. The redshift coverage of these data-sets is $0.0012 \lesssim z \lesssim 2.55$, and the sparse region beyond $z > 1.4$ is complemented by the data from HII galaxies. The inclusion of HII galaxies data has shown improvements in parameter constraints, even though its use in constraining $f(R)$ models is not yet widespread. In light of the so-called “Hubble tension”, we have also examined cases with vis-a-vis without a SH0ES prior for H_0 — a feature which is very often lacking in many earlier studies (see references in Sec I). It is noteworthy to find that incorporating this prior for H_0 , based on local measurements, generally leads to reduction in the differences between predictions of $f(R)$ models and the Λ CDM

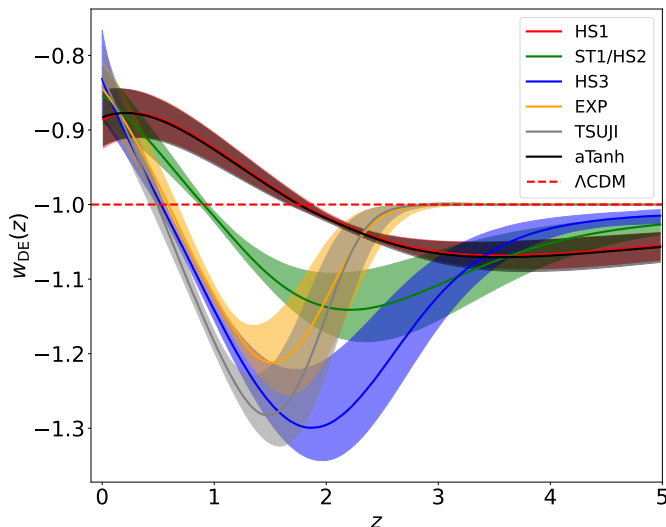


FIG. 19. Evolution of EoS parameter of the “effective geometric dark energy” for all $f(R)$ models obtained from the data-set SBCHII. Different colored solid lines show median values for different models as indicated by legends whereas with same color shaded areas show 1-sigma confidence interval.

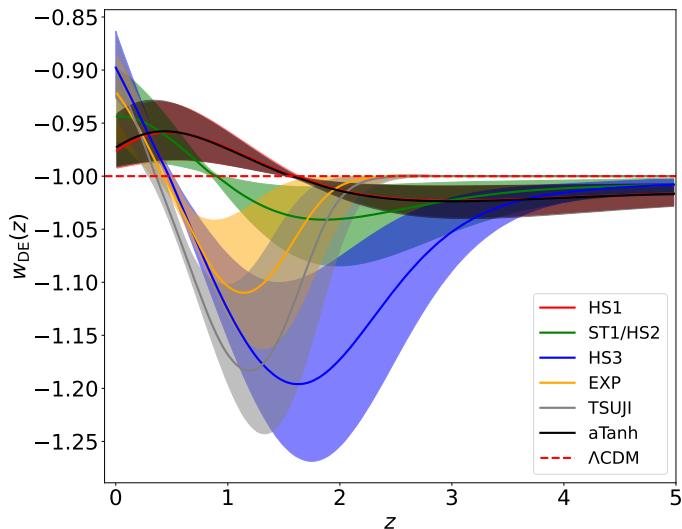


FIG. 20. Evolution of EoS parameter of the “effective geometric dark energy” for all $f(R)$ models obtained from the data-set SBCHII H_0 . Different colored solid lines show median values for different models as indicated by legends whereas shaded areas with colors show 1-sigma confidence interval.

model

The six viable $f(R)$ models examined in this study are the Hu-Sawicki model with $n_{\text{HS}} = 1, 3$, the Starobinsky model ($n_S = 1$), the exponential, the Tsujikawa and the arcTanh model. Reparametrisation of these $f(R)$ models using the deviation parameter b , shows that in the limit $b \rightarrow 0$, these models converge to the standard Λ CDM model. Each of these $f(R)$ models is characterized

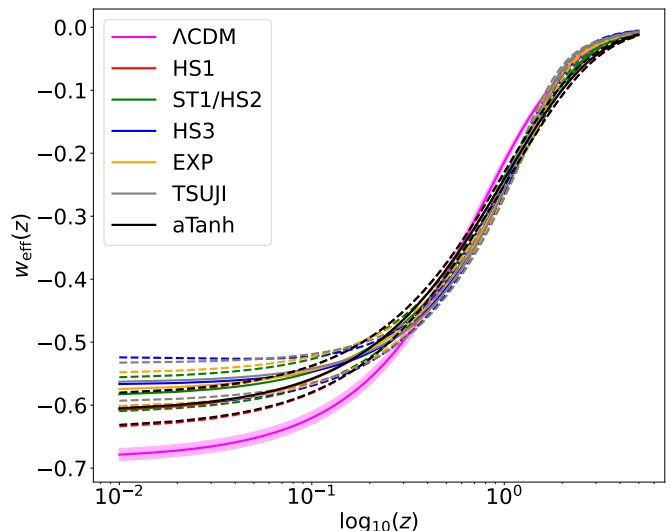


FIG. 21. Evolution of the total EoS parameter for all $f(R)$ models and the Λ CDM model obtained from the data-set SBCHII. Different colored solid lines show median values for different models as indicated by legends whereas dashed lines (or shaded area) with colors show 1-sigma confidence interval. For better contrast we choose $\log_{10}(z)$ as independent variable.

by three parameters: the deviation parameter b , the present-epoch values of the matter density parameter Ω_{m0} , and the Hubble parameter H_0 .

Regardless of whether the SH0ES prior for H_0 is considered, the Ω_{m0} values for all the examined models fall within the 1-2 sigma range of the Planck constrained value ($\Omega_{m0, \text{Planck}} = 0.315 \pm 0.007$) or, conversely, the Planck value lies within the 1-2 sigma range of the model values. When no SH0ES prior for H_0 is considered, the fitted values of H_0 for the models are also within the 1-2 sigma range of that from the Planck constraint ($H_{0, \text{Planck}} = 67.4 \pm 0.5$), or alternatively, the Planck value lies within the 1-2 sigma range of the fitted model values. When incorporating the SH0ES prior on H_0 , the fitted model values of H_0 tend to lie within the 2-3 sigma range on the lower side of the SH0ES measurement of $H_{0, \text{SH0ES}} = 73.04 \pm 1.04$. An additional impact resulting from the SH0ES prior on H_0 is the tightening of constraints on all three model parameters for all the models and data-sets.

In our study, we have found instances of all the investigated $f(R)$ models where the deviation parameter b significantly deviates from zero, indicating that $b = 0$ is only marginally allowed. It is worth highlighting that these cases also correspond to the situations where ΔAIC and/or ΔBIC based analysis suggest that the $f(R)$ models are (very) strongly favoured over the Λ CDM model. Based on our knowledge of previous studies (referred in Sec I), it can be stated that up until

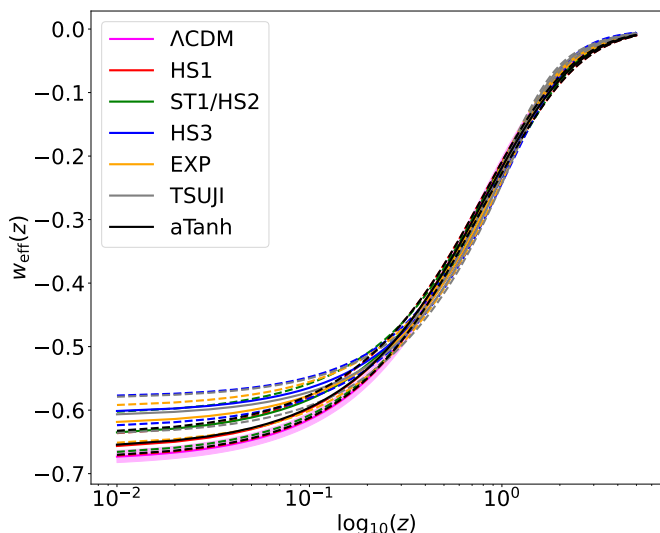


FIG. 22. Evolution of the total EoS parameter for all $f(R)$ models and the Λ CDM model obtained from the data-set SBCHI H_0 . Different colored solid lines show median values for different models as indicated by legends whereas dashed lines (or shaded area) with colors show 1-sigma confidence interval. For better contrast we choose $\log_{10}(z)$ as independent variable.

now, the support for $f(R)$ models has mainly been weak or positive (based on Δ AIC and/or Δ BIC). However, our current research yields (very) strong support for $f(R)$ models, along with support for non-zero values of the deviation parameter b . This indicates that the viability of $f(R)$ models have not yet been ruled out by the available cosmological data sets.

We find that the relevant quantities characterizing the (accelerated) expansion of the universe — z_t , $w_{\text{eff},0}$, and $w_{\text{DE},0}$ — estimated in this study are compatible with their model-independent estimates from earlier works. All the models examined in this study, predict that the universe underwent a transition from a decelerated phase of expansion to an accelerated phase of expansion in the recent past, occurring at $z_t \sim 0.5 - 1$. Furthermore, the current values of w_{DE} fall within the quintessential region, having recently crossed over from the phantom region (around $z \sim 0.5 - 2$, depending on the specific models).

The instances of strong evidence in favor of $f(R)$ models accompanied by clear non-zero b (or only very marginal allowance for $b = 0$), agreements between the derived quantities z_t , $w_{\text{eff},0}$, and $w_{\text{DE},0}$ here and their expected values from model-independent predictions, suggest that the analyzed cosmological data sets allow room for the consideration of viability of $f(R)$ models as an explanation for the observed late time cosmic acceleration. In fact, it would be worthwhile to conduct even further investigations of these models using future data sets.

DATA AVAILABILITY

The observed cosmological data such as SNIa, CC, BAO, HII starburst galaxies and local measurement of H_0 are publicly available — the references to which are cited in the text. The simulated data generated in this work are available from the corresponding author, KR, upon reasonable request.

ACKNOWLEDGEMENTS

K.R. would like to thank HoD, Dept. of Comp. Sc., RKMVERI, for providing computational facilities. A.C. would like to thank Indian Institute of Technology, Kanpur, for supporting this work by means of Institute Post-Doctoral Fellowship (Ref. No. DF/PDF197/2020-IITK/970).

Appendix A: The Modified Friedmann Equations as a System of First Order ODEs

The strategies employed to solve the system of Eqs. 7, 10 and 11 have been proposed and utilized in various earlier studies [19, 24, 94–98]. Although there has been proposals for using model-dependent schemes [19, 25] too, in our current work, we were able to obtain stable solutions for all the considered $f(R)$ models using a single scheme. This scheme involves transforming the ODEs into a system of first-order ODEs using dynamical variables, which avoids numerical instability and reduces overall computational cost. Based on the literature reviewed, we define the following dimensionless variables

$$\begin{aligned} X_1 &= \frac{R}{6(\eta H_0^\Lambda)^2}, \quad X_2 = \frac{\dot{R}F'}{(\eta H_0^\Lambda)F}, \quad X_3 = \frac{f}{6(\eta H_0^\Lambda)^2 F}, \\ O_m &= \frac{\Omega_{m0}^\Lambda (1+z)^3}{\eta^2 F}, \quad O_r = \frac{\Omega_{r,0}^\Lambda (1+z)^4}{\eta^2 F}, \\ H &= \eta H_0^\Lambda, \quad \Gamma = \frac{F}{RF'}, \quad r = \frac{R}{R_*}, \end{aligned} \quad (\text{A1})$$

where z denotes redshift, Ω_{m0}^Λ and $\Omega_{r,0}^\Lambda$ respectively represent the matter and radiation density at present epoch, and $\eta = H/H_0^\Lambda$. The superscript Λ denotes quantities inferred in a Λ CDM paradigm. The parameter R_* has the dimension of Ricci scalar, and its value gets fixed by the choice of a specific $f(R)$ model (e.g. for the Hu-Sawicki model $R_* \equiv \mu^2$, for the Starobinsky model $R_* \equiv R_S$, for the exponential model $R_* \equiv 1/\beta$ and for the Tsujikawa model $R_* \equiv R_T$). The fact that any $f(R)$ model is expected to approach Λ CDM cosmology at sufficiently high redshifts (say z^i , initial redshift) allows us to set the necessary initial conditions for the ODE system. The determination of z^i will be discussed later in this section.

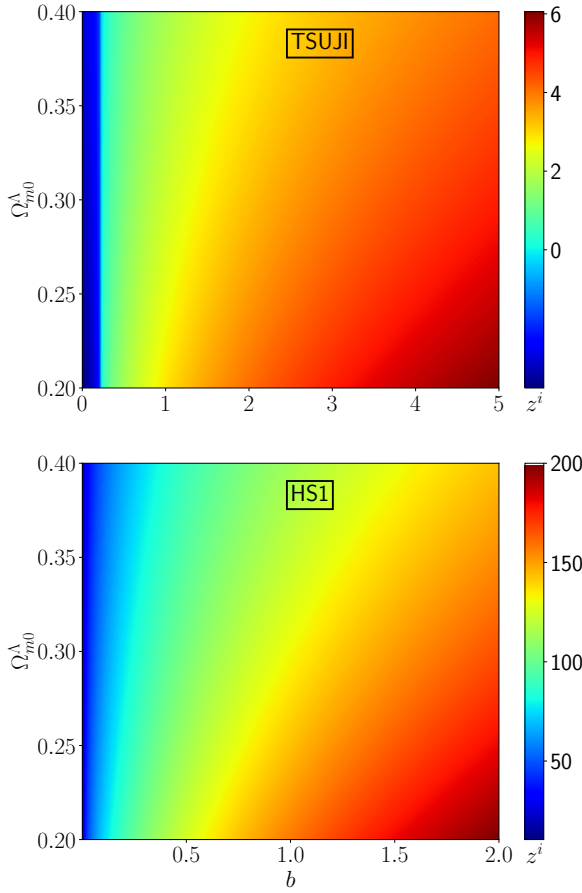


FIG. 23. The color projection plot of relation Eq. A12 which show $z^i(\Omega_{m0}^\Lambda, b)$ below which the solutions need to be switched from the Λ CDM to $f(R)$ (at z^i we obtain the initial conditions for the ODE system Eqs. A5 to A10 from Λ CDM approximations). Top panel is plot is for the Tsujikawa model and the bottom panel plot is for the Hu-Sawicki model($n_{\text{HS}} = 1$).

In terms of the above dynamical/dimensionless variables defined in Eq. A1, the Eqs. 7 and 10 can be written as

$$\frac{d\eta}{dz} = \frac{\eta}{(1+z)}(2 - X_1), \quad (\text{A2})$$

and,

$$1 = O_m + O_r + X_1 - X_2 - X_3, \quad (\text{A3})$$

respectively. Thus it becomes evident from the expression in Eq. A3 that it serves the purpose of setting the initial conditions and monitoring the solutions at each steps of integration. We can also express the equation for effective geometric dark energy(Eq. 15) in terms of above variables as

$$w_{\text{DE}} = \frac{w_{\text{tot}} - O_r F/3}{1 - (O_m + O_r)F}. \quad (\text{A4})$$

We further define $N = -\log(1+z)$, which allows us to rewrite the system of first-order ODEs that need to be

solved as follows:

$$\frac{dX_1}{dN} = X_1 (X_2 \Gamma - 2X_1 + 4), \quad (\text{A5})$$

$$\frac{dX_2}{dN} = (O_m + 2X_1 - X_2 - 4X_3 - X_1 X_2 - X_2^2), \quad (\text{A6})$$

$$\frac{dX_3}{dN} = (X_1 X_2 \Gamma - X_2 X_3 + 4X_3 - 2X_1 X_3), \quad (\text{A7})$$

$$\frac{dO_m}{dN} = -O_m(-1 + 2X_1 + X_2), \quad (\text{A8})$$

$$\frac{dr}{dN} = X_2 \Gamma r, \quad (\text{A9})$$

and,

$$\frac{dO_r}{dN} = -O_r(2X_1 + X_2), \quad (\text{A10})$$

where $\Gamma = F/(RF')$. We choose $\Omega_{r,0}^\Lambda = 2.9656 \times 10^{-4} \Omega_{m0}^\Lambda$, and with this choice, Eq. A10 becomes redundant as it reduces to Eq. A8. Therefore, we only need to solve the system of ODEs consisting of Eqs. A5 to A9 and not Eq. A10. The reason for considering $\Omega_{r,0}^\Lambda$ (and hence O_r) will be explained later in this section. Ultimately, by solving the above system, we obtain $H = \sqrt{rR_*/(6X_1)}$. Using this expression for $H(z)$, we can determine other cosmological observables as defined in Sec. IV. While we perform model-fitting with parameters Ω_{m0}^Λ , b and H_0^Λ , we eventually obtain the relevant parameters for the $f(R)$ models, **viz.** $\Omega_{m0}^{f(R)}$, b , and $H_0^{f(R)}$ (using Eq. 24), where $H_0^{f(R)}$ is the numerical solution of the aforementioned H at $z = 0$.

The initial conditions needed to solve the system of Eqs. A5 to A9 are given by

$$\begin{aligned} X_1^i &= \frac{\Omega_{m0}^\Lambda(1+z^i)^3 + 4\Omega_{\Lambda,0}^\Lambda}{2\eta^{i2}}, \\ X_2^i &= 0, \\ X_3^i &= \frac{\Omega_{m0}^\Lambda(1+z^i)^3 + 2\Omega_{\Lambda,0}^\Lambda}{2\eta^{i2}}, \\ O_m^i &= 1 - O_r^i - X_1^i + X_2^i + X_3^i, \\ r^i &= \frac{3(H_0^\Lambda)^2}{R_*} [(\Omega_{m0}^\Lambda(1+z^i)^3 + 4\Omega_{\Lambda,0}^\Lambda)], \end{aligned} \quad (\text{A11})$$

where $\eta^{i2} = \Omega_{m0}^\Lambda(1+z^i)^3 + \Omega_{r,0}^\Lambda(1+z^i)^4 + \Omega_{\Lambda,0}^\Lambda$, $O_r^i = \frac{\Omega_{r,0}^\Lambda(1+z^i)^4}{\eta^{i2}}$ and $\Omega_{\Lambda,0}^\Lambda = (1 - \Omega_{m0}^\Lambda - \Omega_{r,0}^\Lambda)$.

In order to estimate z_i we set $f(R(z_i)) = R - 2\Lambda(1 - \epsilon)$ where $\epsilon \ll 1$. Here the expressions for R and Λ correspond to those in the Λ CDM cosmology. With this one obtains the following expression for z_i (see [19, 24] for derivation):

$$z_i = \left[\frac{4\Omega_{\Lambda,0}^\Lambda}{\Omega_{m0}^\Lambda} \left(\frac{b}{4\nu_f} - 1 \right) \right]^{1/3} - 1, \quad (\text{A12})$$

where ν_f for different models (f) are given by following

expressions:

$$\begin{aligned} \nu_{\text{HS}} &= \frac{1}{(1/\epsilon - 1)^{1/n_{\text{HS}}}}, \quad \nu_{\text{ST}} = \sqrt{(1/\epsilon)^{1/n_{\text{S}}} - 1}, \\ \nu_{\text{E}} &= -1/\ln \epsilon, \quad \nu_{\text{T}} = 1/\text{arctanh}(1 - \epsilon), \quad \nu_{\text{aTanh}} \approx \epsilon. \end{aligned} \quad (\text{A13})$$

If, during MCMC sampling, the value of z^i for a particular set of parameters $(\Omega_{\text{m}0}^{\Lambda}, b)$ is found to be smaller than the maximum redshift (z_{max}) of the data, we switch from the Λ CDM solution within the range $[z^i, z_{\text{max}}]$ to the $f(R)$ solution for the range $[0, z^i]$ at z^i . Depending on $f(R)$ models, for some samples of $(\Omega_{\text{m}0}^{\Lambda}, b)$ Eq. A12 may yield $z^i \leq 0$. This indicates that for such situations the Λ CDM cosmology is the solution for all $z > 0$ (for example, see the top panel plot in Fig. 23).

Prior to running the MCMC code for a large number of samples, we conducted a preliminary run with a smaller sample size (approximately 50,000) to determine suitable values for ϵ . This avoids long computation times without compromising with accuracy of the results. Based on the findings of this pilot project, we choose $\epsilon = 10^{-10}$ for the exponential and the Tsujikawa models, $\epsilon = 10^{-8}$ for the Starobinsky model and the Hu-Sawicki model with $n_{\text{HS}} = 3$, and $\epsilon = 10^{-6}$ for the Hu-Sawicki model with $n_{\text{HS}} = 1$ and the aTanh model.

We have included a color projection plot in Fig. 23 illustrating the relationship described in Eq. A12 for the Tsujikawa model and the Hu-Sawicki model ($n_{\text{HS}} = 1$). From this plot, it can be observed that for some samples of $(\Omega_{\text{m}0}^{\Lambda}, b)$, the value of z^i can reach as high as 200. In such cases, when we have high z^i one must include $\Omega_{\text{r},0}^{\Lambda}$ in the definition of η^i even though $\Omega_{\text{r},0}^{\Lambda}$ is not a free parameter and one has data-set comprising lower redshifts (as in our case). Through our preliminary investigations, we observed that excluding $\Omega_{\text{r},0}^{\Lambda}$ led to numerical instability and inaccuracies when solving the system of ODEs described by Eqs. A5 to A10. Therefore, based on both theoretical principles and our practical experience, we made the decision to include $\Omega_{\text{r},0}^{\Lambda}$ in our analysis.

Appendix B: BAO and CC Data

The data-sets for BAO and CC used in this work is given in the Tables III and IV, respectively. The covariance matrices, taken from respective cited references, for BAO data points 21-25, 27-28 and 29-30, respectively,

are given in the following equations:

$$C_1 = \begin{bmatrix} 624.707 & 23.729 & 325.332 & 8.34963 & 157.386 & 3.57778 \\ 23.729 & 5.60873 & 11.6429 & 2.33996 & 6.39263 & 0.968056 \\ 325.332 & 11.6429 & 905.777 & 29.3392 & 515.271 & 14.1013 \\ 8.34963 & 2.33996 & 29.3392 & 5.42327 & 16.1422 & 2.85334 \\ 157.386 & 6.39263 & 515.271 & 16.1422 & 1375.12 & 40.4327 \\ 3.57778 & 0.968056 & 14.1013 & 2.85334 & 40.4327 & 6.25936 \end{bmatrix}, \quad (\text{B1})$$

TABLE III. The BAO data collected from many cited sources. The three needed covariance matrices for data-points (i)21-25 (ii)27-28 and (iii)29-30 can be found in the respective references and are given here in Eqs. B1, B2, and B3, respectively.

No.	z_{eff}	Value	Observable	Reference
1	0.106	0.336 ± 0.015	r_d/D_V	[51]
2	0.275	0.1390 ± 0.0037	r_d/D_V	[52]
3	0.122	3.65 ± 0.115	D_V/r_d	[60]
4	0.15	4.47 ± 0.168	D_V/r_d	[61]
5	0.32	8.47 ± 0.167	D_V/r_d	[54]
6	0.35	8.88 ± 0.17	D_V/r_d	[53]
7	0.44	11.55 ± 0.559	D_V/r_d	[62]
8	0.57	13.67 ± 0.22	D_V/r_d	[55]
9	0.6	14.95 ± 0.68	D_V/r_d	[62]
10	0.72	16.08 ± 0.406	D_V/r_d	[56]
11	0.73	16.93 ± 0.579	D_V/r_d	[62]
12	1.52	26.0 ± 0.995	D_V/r_d	[63]
13	0.54	9.212 ± 0.41	D_A/r_d	[57]
14	0.697	10.39 ± 0.496	D_A/r_d	[58]
15	0.81	10.75 ± 0.43	D_A/r_d	[64]
16	0.874	11.37 ± 0.693	D_A/r_d	[58]
17	2.3	9.07 ± 0.31	D_H/r_d	[65]
18	2.34	8.86 ± 0.29	D_H/r_d	[59]
19	2.36	9.0 ± 0.3	$c/(r_d H)$	[67]
20	2.4	36.6 ± 1.2	D_M/r_d	[66]
21	0.38	1512.39	$D_M(r_{d,\text{fid}}/r_d)$	[68]
22	0.38	81.2087	$H(z)(r_d/r_{d,\text{fid}})$	[68]
23	0.51	1975.22	$D_M(r_{d,\text{fid}}/r_d)$	[68]
24	0.51	90.9029	$H(z)(r_d/r_{d,\text{fid}})$	[68]
25	0.61	2306.68	$D_M(r_{d,\text{fid}}/r_d)$	[68]
26	0.61	98.9647	$H(z)(r_d/r_{d,\text{fid}})$	[68]
27	0.698	17.65 ± 0.3	D_M/r_d	[69]
28	0.698	19.77 ± 0.47	D_H/r_d	[69]
29	1.48	13.23 ± 0.47	D_H/r_d	[70]
30	1.48	30.21 ± 0.79	D_M/r_d	[70]

$$C_2 = \begin{bmatrix} 0.0911 & -0.0338 \\ -0.0338 & 0.22 \end{bmatrix}, \quad (\text{B2})$$

and,

$$C_3 = \begin{bmatrix} 0.3047 & 0.1707 \\ 0.1707 & 0.6373 \end{bmatrix}. \quad (\text{B3})$$

[1] S. Perlmutter et al. Discovery of a supernova explosion at half the age of the Universe and its cosmological implications. *Nature*, 391:51–54, 1998. doi:10.1038/34124.

[2] S. Perlmutter et al. Measurements of Ω and Λ from 42 high redshift supernovae. *Astrophys. J.*, 517:565–586, 1999. doi:10.1086/307221.

TABLE IV. The CC data collected from many cited sources.

z	$H(z)$	$\sigma_{H(z)}$	Reference
0.07	69.0	19.6	[44]
0.09	69	12	[41]
0.12	68.6	26.2	[44]
0.17	83	8	[41]
0.179	75	4	[46]
0.199	75	5	[46]
0.20	72.9	29.6	[44]
0.27	77	14	[41]
0.28	88.8	36.6	[44]
0.352	83	14	[46]
0.38	83	13.5	[42]
0.4	95	17	[41]
0.4004	77	10.2	[42]
0.425	87.1	11.2	[42]
0.445	92.8	12.9	[42]
0.47	89.0	49.6	[47]
0.4783	80.9	9	[42]
0.48	97	62	[45]
0.593	104	13	[46]
0.68	92	8	[46]
0.75	98.8	33.6	[48]
0.781	105	12	[46]
0.875	125	17	[46]
0.88	90	40	[45]
0.9	117	23	[41]
1.037	154	20	[46]
1.3	168	17	[41]
1.363	160	33.6	[43]
1.43	177	18	[41]
1.53	140	14	[41]
1.75	202	40	[41]
1.965	186.5	50.4	[43]

[3] Brian P. Schmidt et al. The High Z supernova search: Measuring cosmic deceleration and global curvature of the universe using type Ia supernovae. *Astrophys. J.*, 507:46–63, 1998. doi:10.1086/306308.

[4] Adam G. Riess et al. Observational evidence from supernovae for an accelerating universe and a cosmological constant. *Astron. J.*, 116:1009–1038, 1998. doi:10.1086/300499.

[5] Daniel J. Eisenstein et al. Detection of the Baryon Acoustic Peak in the Large-Scale Correlation Function of SDSS Luminous Red Galaxies. *Astrophys. J.*, 633:560–574, 2005. doi:10.1086/466512.

[6] Will J. Percival et al. Measuring the matter density using baryon oscillations in the SDSS. *Astrophys. J.*, 657:51–55, 2007. doi:10.1086/510772.

[7] D. N. Spergel et al. Wilkinson Microwave Anisotropy Probe (WMAP) three year results: implications for cosmology. *Astrophys. J. Suppl.*, 170:377, 2007. doi:10.1086/513700.

[8] G. Hinshaw et al. Five-Year Wilkinson Microwave Anisotropy Probe (WMAP) Observations: Data Processing, Sky Maps, and Basic Results. *Astrophys. J. Suppl.*, 180:225–245, 2009. doi:10.1088/0067-0049/180/2/225.

[9] P. A. R. Ade et al. Planck 2013 results. XVI. Cosmological parameters. *Astron. Astrophys.*, 571:A16, 2014. doi:10.1051/0004-6361/201321591.

[10] P. A. R. Ade et al. Planck 2015 results. XIII. Cosmological parameters. *Astron. Astrophys.*, 594:A13, 2016. doi:10.1051/0004-6361/201525830.

[11] Shaun Cole et al. The 2dF Galaxy Redshift Survey: Power-spectrum analysis of the final dataset and cosmological implications. *Mon. Not. Roy. Astron. Soc.*, 362:505–534, 2005. doi:10.1111/j.1365-2966.2005.09318.x.

[12] Will J. Percival et al. The shape of the SDSS DR5 galaxy power spectrum. *Astrophys. J.*, 657:645–663, 2007. doi:10.1086/510615.

[13] Ivaylo Zlatev, Li-Min Wang, and Paul J. Steinhardt. Quintessence, cosmic coincidence, and the cosmological constant. *Phys. Rev. Lett.*, 82:896–899, 1999. doi:10.1103/PhysRevLett.82.896.

[14] Jerome Martin. Everything You Always Wanted To Know About The Cosmological Constant Problem (But Were Afraid To Ask). *Comptes Rendus Physique*, 13:566–665, 2012. doi:10.1016/j.crhy.2012.04.008.

[15] Shinji Tsujikawa. Quintessence: A Review. *Class. Quant. Grav.*, 30:214003, 2013. doi:10.1088/0264-9381/30/21/214003.

[16] C. Armendariz-Picon, Viatcheslav F. Mukhanov, and Paul J. Steinhardt. Essentials of k essence. *Phys. Rev. D*, 63:103510, 2001. doi:10.1103/PhysRevD.63.103510.

[17] Spyros Basilakos, Savvas Nesseris, and Leandros Perivolaropoulos. Observational constraints on viable $f(R)$ parametrizations with geometrical and dynamical probes. *Phys. Rev. D*, 87(12):123529, 2013. doi:10.1103/PhysRevD.87.123529.

[18] Rafael C. Nunes, Supriya Pan, Emmanuel N. Saridakis, and Everton M. C. Abreu. New observational constraints on $f(R)$ gravity from cosmic chronometers. *JCAP*, 01:005, 2017. doi:10.1088/1475-7516/2017/01/005.

[19] Sergei D. Odintsov, Diego Sáez-Chillón Gómez, and German S. Sharov. Is exponential gravity a viable description for the whole cosmological history? *Eur. Phys. J. C*, 77(12):862, 2017. doi:10.1140/epjc/s10052-017-5419-z.

[20] Judit Pérez-Romero and Savvas Nesseris. Cosmological constraints and comparison of viable $f(R)$ models. *Phys. Rev. D*, 97(2):023525, 2018. doi:10.1103/PhysRevD.97.023525.

[21] Rocco D’Agostino and Rafael C. Nunes. Probing observational bounds on scalar-tensor theories from standard sirens. *Phys. Rev. D*, 100(4):044041, 2019. doi:10.1103/PhysRevD.100.044041.

[22] Rocco D’Agostino and Rafael C. Nunes. Measurements of H_0 in modified gravity theories: The role of lensed quasars in the late-time Universe. *Phys. Rev. D*, 101(10):103505, 2020. doi:10.1103/PhysRevD.101.103505.

[23] Sergei D. Odintsov, Diego Sáez-Chillón Gómez, and German S. Sharov. Analyzing the H_0 tension in $F(R)$ gravity models. *Nucl. Phys. B*, 966:115377, 2021. doi:10.1016/j.nuclphysb.2021.115377.

[24] Christine R. Farrugia, Joseph Sultana, and Jergen Mifsud. Spatial curvature in $f(R)$ gravity. *Phys. Rev. D*, 104(12):123503, 2021. doi:10.1103/PhysRevD.104.123503.

[25] Matias Leizerovich, Lucila Kraisselburd, Susana J. Landau, and Claudia G. Scóccola. Testing $f(R)$ gravity models with quasar x-ray and UV fluxes. *Phys. Rev. D*, 105(10):103526, 2022. doi:10.1103/PhysRevD.105.103526.

[26] Joseph Sultana, Manoj K. Yennapureddy, Fulvio Melia, and Demosthenes Kazanas. Constraining $f(R)$ models with cosmic chronometers and the H ii galaxy Hubble diagram. *Mon. Not. Roy. Astron. Soc.*, 514(4):5827–5839,

2022. doi:10.1093/mnras/stac1713.
- [27] Antonio De Felice and Shinji Tsujikawa. $f(R)$ theories. *Living Rev. Rel.*, 13:3, 2010. doi:10.12942/lrr-2010-3.
- [28] Luca Amendola and Shinji Tsujikawa. *Dark Energy: Theory and Observations*. Cambridge University Press, 1 2015. ISBN 978-1-107-45398-2.
- [29] Wayne Hu and Ignacy Sawicki. Models of $f(R)$ Cosmic Acceleration that Evade Solar-System Tests. *Phys. Rev. D*, 76:064004, 2007. doi:10.1103/PhysRevD.76.064004.
- [30] Alexei A. Starobinsky. Disappearing cosmological constant in $f(R)$ gravity. *JETP Lett.*, 86:157–163, 2007. doi:10.1134/S0021364007150027.
- [31] G. Cognola, E. Elizalde, S. Nojiri, S. D. Odintsov, L. Sebastiani, and S. Zerbini. A Class of viable modified $f(R)$ gravities describing inflation and the onset of accelerated expansion. *Phys. Rev. D*, 77:046009, 2008. doi:10.1103/PhysRevD.77.046009.
- [32] Eric V. Linder. Exponential Gravity. *Phys. Rev. D*, 80:123528, 2009. doi:10.1103/PhysRevD.80.123528.
- [33] Yun Chen, Chao-Qiang Geng, Chung-Chi Lee, Ling-Wei Luo, and Zong-Hong Zhu. Constraints on the exponential $f(R)$ model from latest Hubble parameter measurements. *Phys. Rev. D*, 91(4):044019, 2015. doi:10.1103/PhysRevD.91.044019.
- [34] Shinji Tsujikawa. Observational signatures of $f(R)$ dark energy models that satisfy cosmological and local gravity constraints. *Phys. Rev. D*, 77:023507, 2008. doi:10.1103/PhysRevD.77.023507.
- [35] M. M. Phillips. The absolute magnitudes of Type IA supernovae. *Astrophys. J. Lett.*, 413:L105–L108, 1993. doi:10.1086/186970.
- [36] Dan Scolnic et al. The Pantheon+ Analysis: The Full Data Set and Light-curve Release. *Astrophys. J.*, 938(2):113, 2022. doi:10.3847/1538-4357/ac8b7a.
- [37] D. M. Scolnic et al. The Complete Light-curve Sample of Spectroscopically Confirmed SNe Ia from Pan-STARRS1 and Cosmological Constraints from the Combined Pantheon Sample. *Astrophys. J.*, 859(2):101, 2018. doi:10.3847/1538-4357/aab9bb.
- [38] A. Conley et al. Supernova Constraints and Systematic Uncertainties from the First 3 Years of the Supernova Legacy Survey. *Astrophys. J. Suppl.*, 192:1, 2011. doi:10.1088/0067-0049/192/1/1.
- [39] Raul Jimenez and Abraham Loeb. Constraining cosmological parameters based on relative galaxy ages. *Astrophys. J.*, 573:37–42, 2002. doi:10.1086/340549.
- [40] Jun-Jie Wei. Model-independent Curvature Determination from Gravitational-Wave Standard Sirens and Cosmic Chronometers. *Astrophys. J.*, 868(1):29, 2018. doi:10.3847/1538-4357/aae696.
- [41] Joan Simon, Licia Verde, and Raul Jimenez. Constraints on the redshift dependence of the dark energy potential. *Phys. Rev. D*, 71:123001, 2005. doi:10.1103/PhysRevD.71.123001.
- [42] Michele Moresco, Lucia Pozzetti, Andrea Cimatti, Raul Jimenez, Claudia Maraston, Licia Verde, Daniel Thomas, Annalisa Citro, Rita Tojeiro, and David Wilkinson. A 6% measurement of the Hubble parameter at $z \sim 0.45$: direct evidence of the epoch of cosmic re-acceleration. *JCAP*, 05:014, 2016. doi:10.1088/1475-7516/2016/05/014.
- [43] Michele Moresco. Raising the bar: new constraints on the Hubble parameter with cosmic chronometers at $z \sim 2$. *Mon. Not. Roy. Astron. Soc.*, 450(1):L16–L20, 2015. doi:10.1093/mnras/slv037.
- [44] Cong Zhang, Han Zhang, Shuo Yuan, Tong-Jie Zhang, and Yan-Chun Sun. Four new observational $H(z)$ data from luminous red galaxies in the Sloan Digital Sky Survey data release seven. *Res. Astron. Astrophys.*, 14(10):1221–1233, 2014. doi:10.1088/1674-4527/14/10/002.
- [45] Daniel Stern, Raul Jimenez, Licia Verde, Marc Kamionkowski, and S. Adam Stanford. Cosmic Chronometers: Constraining the Equation of State of Dark Energy. I: $H(z)$ Measurements. *JCAP*, 02:008, 2010. doi:10.1088/1475-7516/2010/02/008.
- [46] M. Moresco et al. Improved constraints on the expansion rate of the Universe up to $z \sim 1.1$ from the spectroscopic evolution of cosmic chronometers. *JCAP*, 08:006, 2012. doi:10.1088/1475-7516/2012/08/006.
- [47] A. L. Ratsimbazafy, S. I. Loubser, S. M. Crawford, C. M. Cress, B. A. Bassett, R. C. Nichol, and P. Väisänen. Age-dating Luminous Red Galaxies observed with the Southern African Large Telescope. *Mon. Not. Roy. Astron. Soc.*, 467(3):3239–3254, 2017. doi:10.1093/mnras/stx301.
- [48] Nicola Borghi, Michele Moresco, and Andrea Cimatti. Toward a Better Understanding of Cosmic Chronometers: A New Measurement of $H(z)$ at $z \sim 0.7$. *Astrophys. J. Lett.*, 928(1):L4, 2022. doi:10.3847/2041-8213/ac3fb2.
- [49] Wayne Hu and Naoshi Sugiyama. Small scale cosmological perturbations: An Analytic approach. *Astrophys. J.*, 471:542–570, 1996. doi:10.1086/177989.
- [50] Daniel J. Eisenstein and Wayne Hu. Baryonic features in the matter transfer function. *Astrophys. J.*, 496:605, 1998. doi:10.1086/305424.
- [51] Florian Beutler, Chris Blake, Matthew Colless, D. Heath Jones, Lister Staveley-Smith, Lachlan Campbell, Quentin Parker, Will Saunders, and Fred Watson. The 6dF Galaxy Survey: Baryon Acoustic Oscillations and the Local Hubble Constant. *Mon. Not. Roy. Astron. Soc.*, 416:3017–3032, 2011. doi:10.1111/j.1365-2966.2011.19250.x.
- [52] Will J. Percival et al. Baryon Acoustic Oscillations in the Sloan Digital Sky Survey Data Release 7 Galaxy Sample. *Mon. Not. Roy. Astron. Soc.*, 401:2148–2168, 2010. doi:10.1111/j.1365-2966.2009.15812.x.
- [53] Nikhil Padmanabhan, Xiaoying Xu, Daniel J. Eisenstein, Richard Scalzo, Antonio J. Cuesta, Kushal T. Mehta, and Eyal Kazin. A 2 per cent distance to $z=0.35$ by reconstructing baryon acoustic oscillations - I. Methods and application to the Sloan Digital Sky Survey. *Mon. Not. Roy. Astron. Soc.*, 427(3):2132–2145, 2012. doi:10.1111/j.1365-2966.2012.21888.x.
- [54] Rita Tojeiro et al. The clustering of galaxies in the SDSS-III Baryon Oscillation Spectroscopic Survey: galaxy clustering measurements in the low redshift sample of Data Release 11. *Mon. Not. Roy. Astron. Soc.*, 440(3):2222–2237, 2014. doi:10.1093/mnras/stu371.
- [55] Lauren Anderson et al. The clustering of galaxies in the SDSS-III Baryon Oscillation Spectroscopic Survey: Baryon Acoustic Oscillations in the Data Release 9 Spectroscopic Galaxy Sample. *Mon. Not. Roy. Astron. Soc.*, 427(4):3435–3467, 2013. doi:10.1111/j.1365-2966.2012.22066.x.
- [56] Julian E. Bautista et al. The SDSS-IV extended Baryon Oscillation Spectroscopic Survey: Baryon Acoustic Oscillations at redshift of 0.72 with the DR14 Luminous Red Galaxy Sample. *Astrophys. J.*, 863:110, 2018. doi:10.3847/1538-4357/aacea5.

- [57] Hee-Jong Seo et al. Acoustic scale from the angular power spectra of SDSS-III DR8 photometric luminous galaxies. *Astrophys. J.*, 761:13, 2012. doi:10.1088/0004-637X/761/1/13.
- [58] Srivatsan Sridhar, Yong-Seon Song, Ashley J. Ross, Rongpu Zhou, Jeffrey A. Newman, Chia-Hsun Chuang, Francisco Prada, Robert Blum, Enrique Gaztañaga, and Martin Landriau. Clustering of LRGs in the DECaLS DR8 Footprint: Distance Constraints from Baryon Acoustic Oscillations Using Photometric Redshifts. *Astrophys. J.*, 904(1):69, 2020. doi:10.3847/1538-4357/abc0f0.
- [59] Victoria de Sainte Agathe et al. Baryon acoustic oscillations at $z = 2.34$ from the correlations of Ly α absorption in eBOSS DR14. *Astron. Astrophys.*, 629:A85, 2019. doi:10.1051/0004-6361/201935638.
- [60] Paul Carter, Florian Beutler, Will J. Percival, Chris Blake, Jun Koda, and Ashley J. Ross. Low Redshift Baryon Acoustic Oscillation Measurement from the Reconstructed 6-degree Field Galaxy Survey. *Mon. Not. Roy. Astron. Soc.*, 481(2):2371–2383, 2018. doi:10.1093/mnras/sty2405.
- [61] Ashley J. Ross, Lado Samushia, Cullan Howlett, Will J. Percival, Angela Burden, and Marc Manera. The clustering of the SDSS DR7 main Galaxy sample – I. A 4 per cent distance measure at $z = 0.15$. *Mon. Not. Roy. Astron. Soc.*, 449(1):835–847, 2015. doi:10.1093/mnras/stv154.
- [62] Eyal A. Kazin et al. The WiggleZ Dark Energy Survey: improved distance measurements to $z = 1$ with reconstruction of the baryonic acoustic feature. *Mon. Not. Roy. Astron. Soc.*, 441(4):3524–3542, 2014. doi:10.1093/mnras/stu778.
- [63] Metin Ata et al. The clustering of the SDSS-IV extended Baryon Oscillation Spectroscopic Survey DR14 quasar sample: first measurement of baryon acoustic oscillations between redshift 0.8 and 2.2. *Mon. Not. Roy. Astron. Soc.*, 473(4):4773–4794, 2018. doi:10.1093/mnras/stx2630.
- [64] T. M. C. Abbott et al. Dark Energy Survey Year 1 Results: Measurement of the Baryon Acoustic Oscillation scale in the distribution of galaxies to redshift 1. *Mon. Not. Roy. Astron. Soc.*, 483(4):4866–4883, 2019. doi:10.1093/mnras/sty3351.
- [65] Julian E. Bautista et al. Measurement of baryon acoustic oscillation correlations at $z = 2.3$ with SDSS DR12 Ly α -Forests. *Astron. Astrophys.*, 603:A12, 2017. doi:10.1051/0004-6361/201730533.
- [66] Hélion du Mas des Bourboux et al. Baryon acoustic oscillations from the complete SDSS-III Ly α -quasar cross-correlation function at $z = 2.4$. *Astron. Astrophys.*, 608:A130, 2017. doi:10.1051/0004-6361/201731731.
- [67] Andreu Font-Ribera et al. Quasar-Lyman α Forest Cross-Correlation from BOSS DR11 : Baryon Acoustic Oscillations. *JCAP*, 05:027, 2014. doi:10.1088/1475-7516/2014/05/027.
- [68] Shadab Alam et al. The clustering of galaxies in the completed SDSS-III Baryon Oscillation Spectroscopic Survey: cosmological analysis of the DR12 galaxy sample. *Mon. Not. Roy. Astron. Soc.*, 470(3):2617–2652, 2017. doi:10.1093/mnras/stx721.
- [69] Julian E. Bautista et al. The Completed SDSS-IV extended Baryon Oscillation Spectroscopic Survey: measurement of the BAO and growth rate of structure of the luminous red galaxy sample from the anisotropic correlation function between redshifts 0.6 and 1. *Mon. Not. Roy. Astron. Soc.*, 500(1):736–762, 2020. doi:10.1093/mnras/staa2800.
- [70] Richard Neveux et al. The completed SDSS-IV extended Baryon Oscillation Spectroscopic Survey: BAO and RSD measurements from the anisotropic power spectrum of the quasar sample between redshift 0.8 and 2.2. *Mon. Not. Roy. Astron. Soc.*, 499(1):210–229, 2020. doi:10.1093/mnras/staa2780.
- [71] Andoni Aizpuru, Rubén Arjona, and Savvas Nesseris. Machine learning improved fits of the sound horizon at the baryon drag epoch. *Phys. Rev. D*, 104(4):043521, 2021. doi:10.1103/PhysRevD.104.043521.
- [72] Ana Luisa González-Morán, Ricardo Chávez, Elena Terlevich, Roberto Terlevich, David Fernández-Arenas, Fabio Bresolin, Manolis Plionis, Jorge Melnick, Spyros Basilakos, and Eduardo Telles. Independent cosmological constraints from high- z H II galaxies: new results from VLT-KMOS data. *Mon. Not. Roy. Astron. Soc.*, 505(1):1441–1457, 2021. doi:10.1093/mnras/stab1385.
- [73] Dawn K. Erb, Charles C. Steidel, Alice E. Shapley, Max Pettini, Naveen A. Reddy, and Kurt L. Adelberger. The Stellar, Gas and Dynamical Masses of Star-Forming Galaxies at $z = 2$. *Astrophys. J.*, 646:107–132, 2006. doi:10.1086/504891.
- [74] Michael V. Maseda et al. The Nature of Extreme Emission Line Galaxies at $z=1-2$: Kinematics and Metallicities from Near-Infrared Spectroscopy. *Astrophys. J.*, 791(1):17, 2014. doi:10.1088/0004-637X/791/1/17.
- [75] Daniel Masters et al. Physical Properties of Emission-Line Galaxies at $z \sim 2$ from Near-Infrared Spectroscopy with Magellan FIRE. *Astrophys. J.*, 785:153, 2014. doi:10.1088/0004-637X/785/2/153.
- [76] Ana Luisa González-Morán, Ricardo Chávez, Roberto Terlevich, Elena Terlevich, Fabio Bresolin, David Fernández-Arenas, Manolis Plionis, Spyros Basilakos, Jorge Melnick, and Eduardo Telles. Independent cosmological constraints from high- z H II galaxies. *Mon. Not. Roy. Astron. Soc.*, 487(4):4669–4694, 2019. doi:10.1093/mnras/stz1577.
- [77] Ricardo Chávez, Manolis Plionis, Spyros Basilakos, Roberto Terlevich, Elena Terlevich, Jorge Melnick, Fabio Bresolin, and Ana Luisa González-Morán. Constraining the dark energy equation of state with H II galaxies. *Mon. Not. Roy. Astron. Soc.*, 462(3):2431–2439, 2016. doi:10.1093/mnras/stw1813.
- [78] N. Aghanim et al. Planck 2018 results. VI. Cosmological parameters. *Astron. Astrophys.*, 641:A6, 2020. doi:10.1051/0004-6361/201833910. [Erratum: *Astron. Astrophys.* 652, C4 (2021)].
- [79] Adam G. Riess et al. A Comprehensive Measurement of the Local Value of the Hubble Constant with 1 km s $^{-1}$ Mpc $^{-1}$ Uncertainty from the Hubble Space Telescope and the SH0ES Team. *Astrophys. J. Lett.*, 934(1):L7, 2022. doi:10.3847/2041-8213/ac5c5b.
- [80] Nicholas Wogan, 2021. URL <https://github.com/Nicholaswogan/numbalsoda>.
- [81] Daniel Foreman-Mackey, David W. Hogg, Dustin Lang, and Jonathan Goodman. emcee: The MCMC Hammer. *Publ. Astron. Soc. Pac.*, 125:306–312, 2013. doi:10.1086/670067.
- [82] Antony Lewis. Getdist: a python package for analysing monte carlo samples, 2019.

- [83] Salvatore Capozziello and Shinji Tsujikawa. Solar system and equivalence principle constraints on $f(R)$ gravity by chameleon approach. *Phys. Rev. D*, 77:107501, 2008. doi:10.1103/PhysRevD.77.107501.
- [84] Xiangyun Fu, Puxun Wu, and Hong Wei Yu. The growth factor of matter perturbations in $f(R)$ gravity. *Eur. Phys. J. C*, 68:271–276, 2010. doi:10.1140/epjc/s10052-010-1324-4.
- [85] H. Akaike. A new look at the statistical model identification. *IEEE Transactions on Automatic Control*, 19(6):716–723, 1974. doi:10.1109/TAC.1974.1100705.
- [86] Gideon Schwarz. Estimating the Dimension of a Model. *The Annals of Statistics*, 6(2):461 – 464, 1978. doi:10.1214/aos/1176344136. URL <https://doi.org/10.1214/aos/1176344136>.
- [87] Andrew R. Liddle. How many cosmological parameters? *Mon. Not. Roy. Astron. Soc.*, 351:L49–L53, 2004. doi:10.1111/j.1365-2966.2004.08033.x.
- [88] Andrew R Liddle. Information criteria for astrophysical model selection. *Mon. Not. Roy. Astron. Soc.*, 377:L74–L78, 2007. doi:10.1111/j.1745-3933.2007.00306.x.
- [89] Kenneth P. Burnham and David R. Anderson. Multi-model inference: Understanding aic and bic in model selection. *Sociological Methods & Research*, 33(2):261–304, 2004. doi:10.1177/0049124104268644. URL <https://doi.org/10.1177/0049124104268644>.
- [90] Nisha Rani, Deepak Jain, Shobhit Mahajan, Amitabha Mukherjee, and Nilza Pires. Transition Redshift: New constraints from parametric and nonparametric methods. *JCAP*, 12:045, 2015. doi:10.1088/1475-7516/2015/12/045.
- [91] J. F. Jesus, R. Valentim, A. A. Escobal, and S. H. Pereira. Gaussian Process Estimation of Transition Redshift. *JCAP*, 04:053, 2020. doi:10.1088/1475-7516/2020/04/053.
- [92] Luisa G. Jaime, Leonardo Patino, and Marcelo Salgado. $f(r)$ cosmology revisited, 2012.
- [93] Kazuharu Bamba, Chao-Qiang Geng, and Chung-Chi Lee. Generic feature of future crossing of phantom divide in viable $f(R)$ gravity models. *JCAP*, 11:001, 2010. doi:10.1088/1475-7516/2010/11/001.
- [94] Luca Amendola, Radouane Gannouji, David Polarski, and Shinji Tsujikawa. Conditions for the cosmological viability of $f(R)$ dark energy models. *Phys. Rev. D*, 75:083504, 2007. doi:10.1103/PhysRevD.75.083504.
- [95] S. Carloni, A. Troisi, and P. K. S. Dunsby. Some remarks on the dynamical systems approach to fourth order gravity. *Gen. Rel. Grav.*, 41:1757–1776, 2009. doi:10.1007/s10714-008-0747-9.
- [96] Mohamed Abdelwahab, Rituparno Goswami, and Peter K. S. Dunsby. Cosmological dynamics of fourth order gravity: A compact view. *Phys. Rev. D*, 85:083511, 2012. doi:10.1103/PhysRevD.85.083511.
- [97] Álvaro de la Cruz-Dombriz, Peter K. S. Dunsby, Surlona Kandhai, and Diego Sáez-Gómez. Theoretical and observational constraints of viable $f(R)$ theories of gravity. *Phys. Rev. D*, 93(8):084016, 2016. doi:10.1103/PhysRevD.93.084016.
- [98] S. D. Odintsov and V. K. Oikonomou. Autonomous dynamical system approach for $f(R)$ gravity. *Phys. Rev. D*, 96(10):104049, 2017. doi:10.1103/PhysRevD.96.104049.